AGU PUBLICATIONS

Tectonics

RESEARCH ARTICLE
10.1002/2017TC004595

Key Points:
- A post-Eocene polyphase tectonic evolution dominated by dextral wrench tectonics is documented for the Doruneh Fault region
- A switch of the paleo-σ1 direction from NW-SE to N-S is documented across the Doruneh Fault region at the Miocene-Pliocene boundary
- Correlation at regional scale suggests a post-Miocene transition from NE escape to NS indentation tectonics in Central Iran

Supporting Information:
- Supporting Information S1

Correspondence to:
F. Rossetti,
federico.rossetti@uniroma3.it

Citation:
Tadayon, M., Rossetti, F., Zattin, M., Nozaem, R., Calzolari, G., Madanipour, S., & Salvini, F. (2017). The post-Eocene evolution of the Doruneh Fault region (Central Iran): The intraplate response to the reorganization of the Arabia-Eurasia collision zone. *Tectonics*, *36*, 3038–3064. https://doi.org/10.1002/2017TC004595

Received 12 APR 2017
Accepted 13 NOV 2017
Accepted article online 20 NOV 2017
Published online 14 DEC 2017
Corrected 20 JAN 2018

This article was corrected on 20 JAN 2018. See the end of the full text for details.

The Post-Eocene Evolution of the Doruneh Fault Region (Central Iran): The Intraplate Response to the Reorganization of the Arabia-Eurasia Collision Zone

Meisam Tadayon[1], Federico Rossetti[1], Massimiliano Zattin[2], Reza Nozaem[3], Gabriele Calzolari[1], Saeed Madanipour[4], and Francesco Salvini[1]

[1]Dipartimento di Scienze, Sezione di Scienze Geologiche, Università degli Studi Roma Tre, Rome, Italy, [2]Dipartimento di Geoscienze, Università di Padova, Italy, [3]School of Geology, College of Science, University of Tehran, Iran, [4]Geology Department, Tarbiat Modares University, Tehran, Iran

Abstract The Cenozoic deformation history of Central Iran has been dominantly accommodated by the activation of major intracontinental strike-slip fault zones, developed in the hinterland domain of the Arabia-Eurasia convergent margin. Few quantitative temporal and kinematic constraints are available from these strike-slip deformation zones, hampering a full assessment of the style and timing of intraplate deformation in Iran and the understanding of the possible linkage to the tectonic reorganization of the Zagros collisional zone. This study focuses on the region to the north of the active trace of the sinistral Doruneh Fault. By combing structural and low-temperature apatite fission track (AFT) and (U-Th)/He (AHe) thermochronology investigations, we provide new kinematic and temporal constraints to the deformation history of Central Iran. Our results document a post-Eocene polyphase tectonic evolution dominated by dextral strike-slip tectonics, whose activity is constrained since the early Miocene in response to an early, NW-SE oriented paleo-σ1 direction. A major phase of enhanced cooling/exhumation is constrained at the Miocene/Pliocene boundary, caused by a switch of the maximum paleo-σ1 direction to N-S. When integrated into the regional scenario, these data are framed into a new tectonic reconstruction for the Miocene-Quaternary time lapse, where strike-slip deformation in the intracontinental domain of Central Iran is interpreted as guided by the reorganization of the Zagros collisional zone in the transition from an immature to a mature stage of continental collision.

1. Introduction

The intraplate deformation zones typically show polyphase tectonic histories whose evolution is commonly assumed to be dynamically linked to the spatiotemporal changes in the mechanical coupling occurring at the plate boundaries (e.g., Ellis, 1996; Molnar, 1988). In particular, the mode (tectonic style and kinematics) of intraplate deformation is chiefly controlled by the distribution and architecture of the inherited structural anisotropies and is modulated by the distribution of the near- and far-field stress regime(s) through time (e.g., Calzolari, Della Seta, et al., 2016; Cloetingh et al., 2005; Cunningham et al., 2003; Di Vincenzo et al., 2013; Holdsworth et al., 1998; Lesti et al., 2008; Niu et al., 2003; Storti et al., 2007; Van Hinsbergen et al., 2015). Definition of the deformation history in intraplate domains in space and time is thus critical to decipher the major episodes of tectonic reorganization at the plate boundaries and to link these to the possible geodynamic causes.

The hinterland domain of the Alpine-Himalayan convergence zone provides the most impressive example of large-scale intraplate deformation on Earth (Hatzfeld & Molnar, 2010). The intraplate deformation developed in response to the compressional stresses resulting from continental collision, transmitted far away from the convergence front (e.g., Molnar & Lyon-Caen, 1988; Reece et al., 2013; Simons et al., 2007; Storti et al., 2003; Van Hinsbergen et al., 2015; Vincent & Allen, 2001; Ziegler et al., 1998). These far-field stresses are responsible for distributed Cenozoic inversion tectonics, mainly accommodated through the development of major intracontinental strike-slip shear belts, as documented in Central Asia, Turkey and Iran (Allen et al., 2004, 2011; Avouac & Tapponnier, 1993; Molnar & Tapponnier, 1975; Van Hinsbergen et al., 2015; Vernant et al., 2004; Walpersdorf et al., 2014).

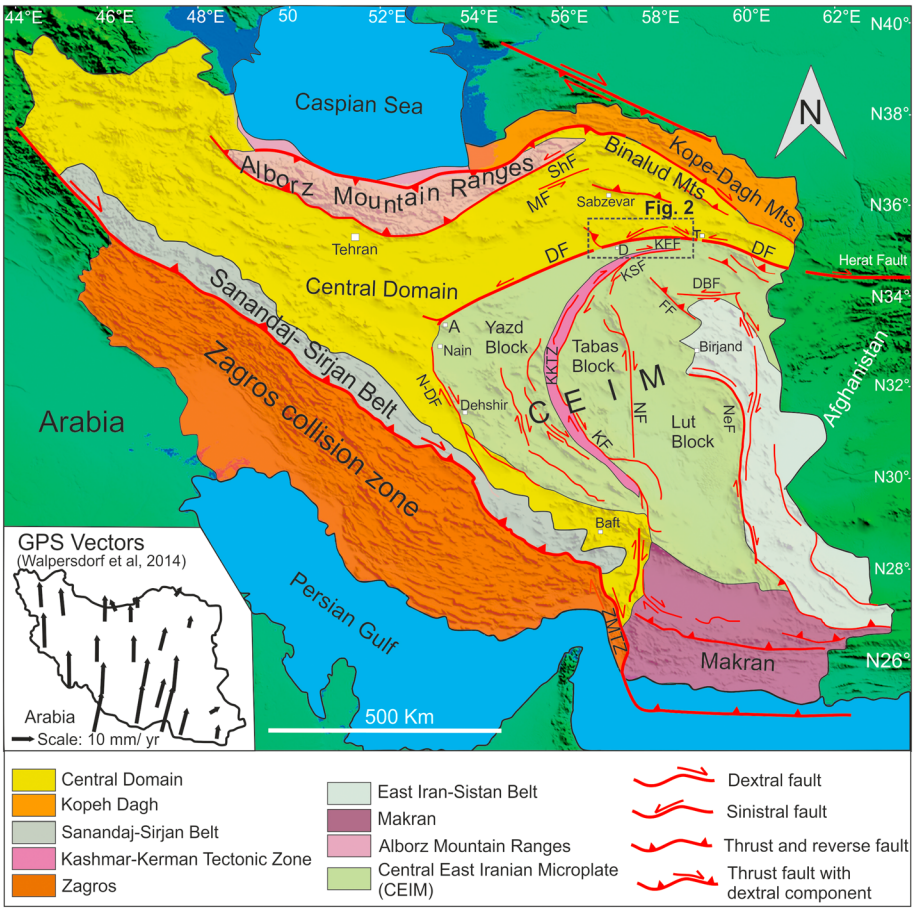

Figure 1. Simplified tectonic map of Iran on the shaded-relief Shuttle Radar Topography Mission (SRTM) image, showing the main tectonic domains and the major strike-slip fault systems accommodating the Arabia-Eurasia convergence. (after Allen et al., 2004, 2011; Berberian, 1983; Berberian & King, 1981; Calzolari, Della Seta, et al., 2016; Morley et al., 2009; Nozaem et al., 2013; Stöcklin & Nabavi, 1973). The inset shows the GPS velocity vectors (black arrows) in Iran relative to stable Eurasia (after Walpersdorf et al., 2014). The black dashed rectangle indicates location of study area, shown in Figure 2. A: Anarak; FF: Ferdows Fault; DBF: Dasht-e-Bayaz Fault; D: Doruneh; DF: Doruneh Fault; KF: Kuhbanan Fault; KFF: Kuh-e-Faghan fault; KKTZ: Kashmar-Kerman tectonic zone; KSF: Kuh-e-Sarhangi fault; MF: Meyamey Fault; NF: Nayband Fault; NeF: Neh Fault; N-DF: Nain-Dehshir Fault; SBF: Shahr-e-Babak fault; ShF: Shahrud Fault; T: Torbat-e-Heydarieh; ZMTZ: Zagros-Makran Transfer Zone.

In Iran, Cenozoic far-field deformation is mainly documented by positive inversion of the Mesozoic basin boundary faults in the Alborz and Kopeh Dagh regions (Allen et al., 2004; Guest, Axen, et al., 2006; Guest et al., 2007; Guest, Stockli, et al., 2006; Hollingsworth et al., 2010; Madanipour et al., 2013, 2017; Robert et al., 2014; Shabanian, Bellier, et al., 2009; Shabanian, Siame, et al., 2009) and by the late Cenozoic activation of major strike-slip deformation zones cutting through the intracontinental domain of the Central East Iranian Microcontinent (CEIM; Figure 1) (Allen et al., 2004; Berberian & King, 1981; Farbod et al., 2011; Foroutan et al., 2012, 2014; Le Dortz et al., 2009, 2011; Meyer & Le Dortz, 2007; Nazari et al., 2009; Walker & Jackson, 2004).

Despite a general agreement on the active kinematic scenario in Central Iran, few quantitative temporal and kinematic constraints are available from the major strike-slip deformation zones cutting across the CEIM, hampering a full assessment of the style and timing of intraplate deformation in Central Iran. Critical in this regard is the long-term evolution of the transcurrent boundaries at the north-western termination of the CEIM, with the sinistral Doruneh Fault (Wellman, 1966; hereafter referred as DF) being commonly considered as the northern mechanical boundary of the deforming CEIM (Berberian, 1974; Farbod et al., 2011, 2016; Fattahi et al., 2007; Javadi et al., 2013, 2015; Stöcklin & Nabavi, 1973; Tchalenko et al., 1973; Walker &

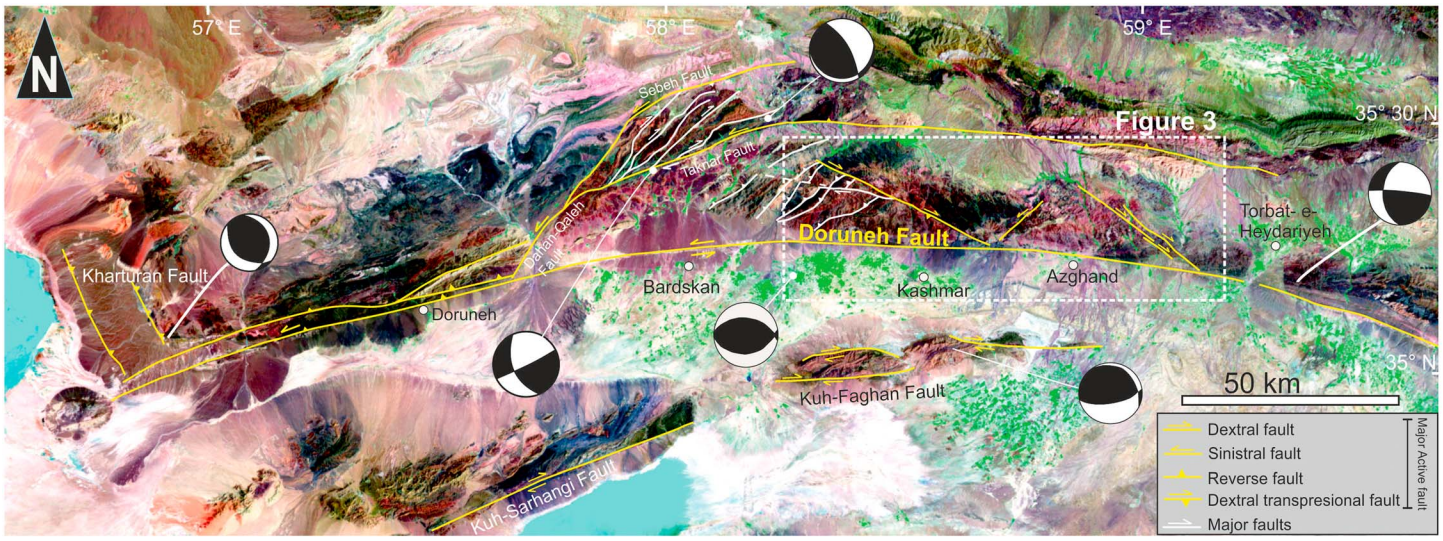

Figure 2. Satellite (Multiresolution Seamless Image Database) image of the northern boundary region of the CEIM, with the available earthquake focal mechanisms (after Farbod et al., 2011) and the major fault systems indicated. The yellow lines indicate the traces of the major active faults (after Berberian, 2014; Farbod et al., 2011; Fattahi et al., 2007), the white lines indicate the main fault traces after Javadi et al. (2013). The dashed rectangle indicates the study area shown in Figure 3.

Jackson, 2004) (Figure 1). A complex paleotectonic evolution has been proposed for this region during the Mesozoic-Cenozoic times, dominated by large-scale crustal wrenching accommodated along the DF and its precursors during segmentation and displacement of Paleo-Tethys suture from NE Iran to the Anarak area (Barrier & Vrielynck, 2008; Berra et al., 2017; Davoudzadeh et al., 1981; Mattei et al., 2012; Soffel et al., 1996; Zanchi et al., 2009; 2015) (Figure 1). In addition, recent papers have documented that kinematic shifts occurred along the DF region in post-Eocene times, from dextral to sinistral (Bagheri et al., 2016; Javadi et al., 2013, 2015), whereas other studies have proposed the onset of strike-slip faulting along the DF at ≤5 Ma (Farbod et al., 2011). Finally, structural, thermochronological and geomorphological evidence just to the south of the active trace of the DF attests to dextral shearing distributed along the northern boundary of the CEIM (along the Kuh-Sarangi and Kuh-e-Faghan faults; Figure 1), also pointing to a different kinematic scenario during the Neogene-Quaternary times (Calzolari, Della Seta, et al., 2016; Calzolari, Rossetti, et al., 2016; Nozaem et al., 2013). This is in line with what is documented to the north of the CEIM, in the transition zone between Alborz and Kopeh Dagh mountain ranges, where a major Pliocene-Quaternary change in the regional stress regime is documented and interpreted as corresponding to a change in the orientation, from Neogene NW-SE to Quaternary NE-SW directed, of the regional maximum shortening direction (Javidfakhr et al., 2011; Shabanian et al., 2012).

Therefore, two main outstanding questions remain regarding the spatiotemporal tectonic evolution of the boundary region to the north of the CEIM: (i) if and when the regional kinematic shift occurred and (ii) which is the link (if any) with the evolution of the convergent plate margin.

Through the integration of structural and low-temperature apatite fission track (AFT) and (U-Th)/He (AHe) thermochronology data, collected to the north of the active trace of the sinistral DF (Figures 2 and 3), this paper aims to provide new kinematic and temporal constrains on the tectonic evolution of the northern boundary of the CEIM. Our results document a polyphase tectonic evolution dominated by dextral wrenching, with a major phase of enhanced cooling/exhumation starting at the Miocene/Pliocene boundary in response to a switch of the regional (paleo-)maximum compression direction from NW-SE to N-S. These data are discussed at regional scale and used to propose a new tectonic scenario for the post-Eocene kinematic evolution of Central Iran.

2. Geological Background

The approximately 2,400 km long Zagros-Bitlis collision zone has been generated by the Arabia-Eurasia convergence during Mesozoic-Cenozoic times (Hatzfeld & Molnar, 2010, and references therein). Collision is commonly estimated to have started at the Eocene-Oligocene boundary (e.g., Agard et al., 2011; Allen &

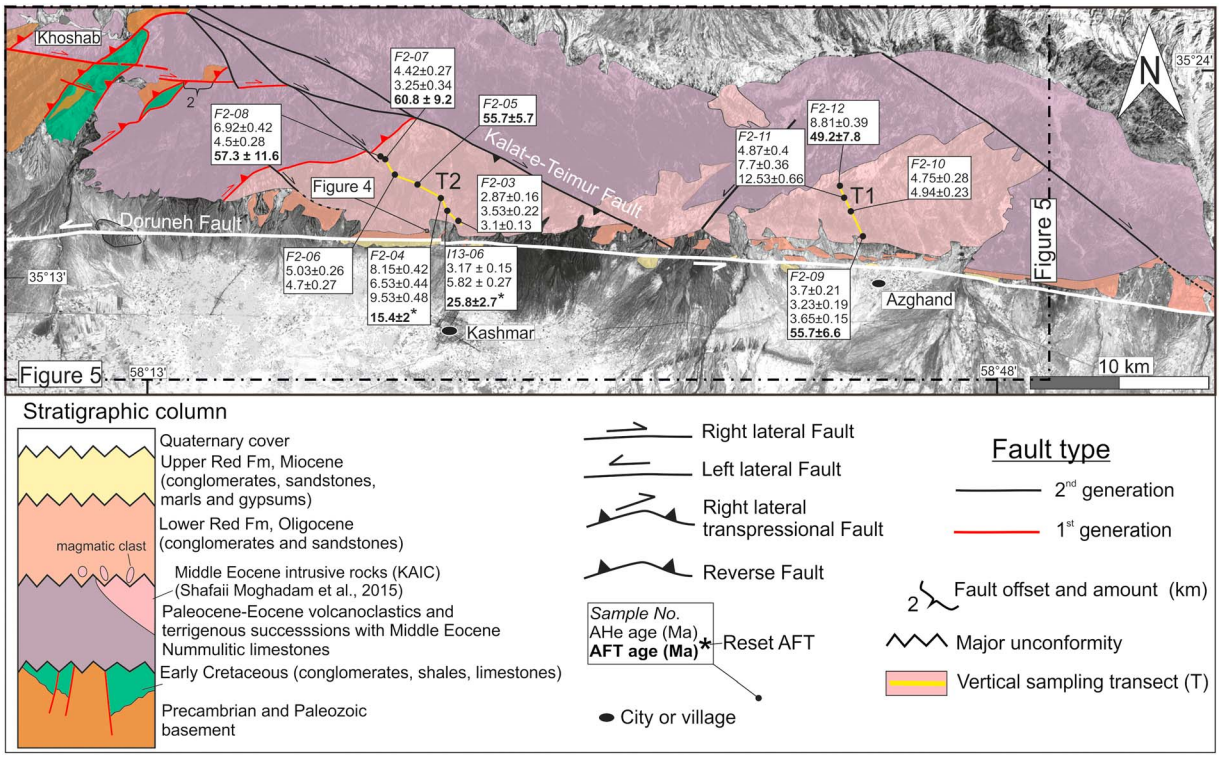

Figure 3. Geological map and synthetic stratigraphic column of the study area (readapted after Vahdati Daneshmand & Nadim, 1999; Ghaemi & Moussavi Herami, 2008; Jafarian et al., 2000; Shahrabi et al., 2005; Taheri et al., 1998) on the Multiresolution Seamless Image Database (MrSID) image. The major fault systems are also indicated. The yellow lines indicate the sampling transects (T1 and T2) for the AFT and AHe thermochronometry, and the black dots the location of the studied samples with the corresponding age results (see Tables 1 and 2). The area shown in Figure 4 is also indicated.

Armstrong, 2008; François et al., 2014; Hafkenscheid et al., 2006; Hessami et al., 2001; Homke et al., 2009, 2010; Karagaranbafghi et al., 2012; Madanipour et al., 2013; McQuarrie et al., 2003; Mouthereau et al., 2012; Robertson et al., 2006; Vincent et al., 2007). A regional increase in collision-related uplift, exhumation and subsidence in adjacent basins, began in the early to middle Miocene, as documented along the Bitlis-Zagros collisional front, the Alborz Mountains, and Central Iran by low-temperature thermochronometric (Axen et al., 2001; Ballato et al., 2013; Calzolari, Della Seta, et al., 2016; François et al., 2014; Gavillot et al., 2010; Guest, Stockli, et al., 2006; Homke et al., 2010; Khadivi et al., 2012; Madanipour et al., 2013; Okay et al., 2010; Verdel et al., 2007), stratigraphic (e.g., Ballato et al., 2008, 2011; Hessami et al., 2001; Guest, Axen, et al., 2006; Guest, Stockli, et al., 2006; Khadivi et al., 2010; Madanipour et al., 2017; Morley et al., 2009; Mouthereau et al., 2007) and structural (e.g., Allen et al., 2004; Mouthereau et al., 2007) evidence.

A widespread tectonic reorganization during late Miocene to early Pliocene is attested in the Iranian region by (i) enhanced exhumation in the Alborz and Talesh mountains (Axen et al., 2001; Madanipour et al., 2013; Rezaeian et al., 2012), (ii) fault kinematic changes along the Zagros belt from a distributed transpressive system (late Miocene) to an across and along-strike partitioned system (early Pliocene (Authemayou et al., 2006; Hatzfeld et al., 2010), (iii) fault kinematic changes in Central Iran along the DF (Javadi et al., 2013, 2015), (iv) the establishment of strike-slip faulting in the Kopeh Dagh region (Javidfakhr et al., 2011; Robert et al., 2014; Shabanian et al., 2010, 2012), (v) oroclinal bending of the Alborz Mountains (Cifelli et al., 2015), and (vi) change in the regional stress field and activation of the Zagros-Makran transfer zone (Regard et al., 2005, 2010). The Miocene-Pliocene boundary also corresponds with the time when the Zagros collisional zone became overthickened and unable to sustain further significant shortening (Allen et al., 2004; Austermann & Iaffaldano, 2013). Such tectonic events are thought to have given rise to in the current regional kinematic configuration (Allen et al., 2004).

The GPS displacement vectors in the Iranian region indicate a NNE motion of the Arabian plate relative to Eurasia, with ~18 mm yr^{-1} in the northwest and increasing to ~25 mm yr^{-1} to the southeast due to

location of the Arabia-Eurasia Euler pole situated in North Africa (McClusky et al., 2003; Reilinger et al., 2006; Sella et al., 2002; Vernant et al., 2004; Walpersdorf et al., 2014). This convergence is mostly absorbed through contractional deformation along the Zagros and by distributed shortening in the north, within the Alborz and Kopeh Dagh Mountain ranges (Figure 1). The obliquity of convergence with respect to the major tectonic boundaries has resulted in a combination of translation and shortening in the intracontinental domains (Authemayou et al., 2006; Calzolari, Della Seta, et al., 2016; Djamour et al., 2010; Ghods et al., 2015; Hollingsworth et al., 2010; Javidfakhr et al., 2011; Mousavi et al., 2015; Nozaem et al., 2013; Ritz et al., 2006; Rizza et al., 2011; Robert et al., 2014; Shabanian et al., 2010, 2012; Shabanian, Bellier, et al., 2009; Shabanian, Siame, et al., 2009; Talebian & Jackson, 2004).

The CEIM is moving northward at 6–13 mm/yr with respect to the stable Afghanistan crust at the eastern edge of the collision zone (Walpersdorf et al., 2014). Such differential motion is largely accommodated by the active strike-slip faults systems that bound and dissect the CEIM, which are organized into N-S dextral (from west to east: the Dehshir, Anar, Nayband–Gowk, and Nehbandan faults) and E-W sinistral (from north to south: Doruneh and Dasht-e Bayaz faults) shear systems (Allen et al., 2004, 2011; Berberian & King, 1981; Farbod et al., 2011; Fattahi et al., 2007; Foroutan et al., 2012; 2014; Le Dortz et al., 2009, 2011; Masson et al., 2007; Meyer & Le Dortz, 2007; Vernant et al., 2004; Walker & Jackson, 2004) (Figure 1), which in most cases are seismically active (Berberian, 2014, and references therein).

3. Geological Setting

The arcuate sinistral DF is commonly regarded as the longest strike-slip fault in intraplate domain of Central Iran, extending from longitude 54°E and 60°30′E, with an along-strike cumulative length in excess of 750 km (Figure 1). According to Javadi et al. (2013), the architecture of the DF is characterized by three main fault strands, western, central, and eastern, respectively. The western strand, also known as Great Kavir Fault, extends from the Doruneh village to central Iran for a cumulative length of approximately 500 km, striking NE-SW and showing sinistral kinematics (Javadi et al., 2015; Stöcklin & Nabavi, 1973; Tchalenko et al., 1973). The central strand, with an E-W strike and sinistral kinematics, extends from the Doruneh village to Torbat-e-Heydaryeh city, with a cumulative along-strike length of approximately 170 km (Farbod et al., 2011, 2016; Fattahi et al., 2007; Javadi et al., 2013; Tchalenko et al., 1973). The eastern strand strikes NW-SE and cuts across the Torbat-e-Heydaryeh region to the Iran-Afghanistan border (Javadi et al., 2013) (Figure 1). Based on geomorphic and structural evidence, Farbod et al. (2011) have proposed internal segmentation of the central part of the DF that, consequently, cannot be regarded as a unique, continuous structure.

At the regional scale, the DF is considered to adsorb a significant amount of the ~15 mm yr^{-1} N-S motion of the CEIM with respect to the stable Afghanistan (Berberian, 2014; Farbod et al., 2011; Fattahi et al., 2007; Vernant et al., 2004). In particular, Farbod et al. (2011), based on GPS data from Masson et al. (2007), has calculated a N-S convergence (across the DF) of 2.2 mm yr^{-1} and 2.5 mm yr^{-1} of E-W sinistral motion. The latter is compatible with the independent geomorphic-derived 2.5 mm yr^{-1} sinistral slip rate proposed by Fattahi et al. (2007). More recently, based on in situ produced ^{10}Be and ^{36}Cl cosmogenic dating, Farbod et al. (2016) have documented a maximum sinistral slip rate of 8.2 ± 2.0 mm yr^{-1} since the late Pleistocene.

The DF region is characterized by moderate seismic activity, as documented by historical and instrumental records (Ambraseys & Melville, 1982; Berberian, 2014; Farbod et al., 2011, 2016; Fattahi et al., 2007; Jackson & McKenzie, 1984; Tchalenko, 1973; Tchalenko et al., 1973). The available focal mechanism solutions ($M \geq 4.5$) are not directly located along the active trace of the DF and the most common focal plane solutions point to thrust faulting on E-W fault planes (see review in Farbod et al., 2011) (Figure 2).

Structural evidence has documented a change in the slip sense from dominant dextral to sinistral kinematics along the western and central fault segment of the DF (Bagheri et al., 2016; Javadi et al., 2013, 2015). In particular, (i) the onset of dextral shearing along the DF region is placed during the Eocene (55.8 Ma), when the DF acted as a major tectonic zone within the Central Iran to accommodate the anticlockwise rigid block rotation of CEIM during Cenozoic times, and (ii) the slip sense inversion to sinistral kinematics in post-late Miocene times (Javadi et al., 2013, 2015). Based on the geomorphic evidence along the active trace of the DF, Farbod et al. (2011) instead proposed a maximum Pliocene age (≤5 Ma) for the initiation of (sinistral) strike-slip faulting along the DF.

Temporal constraints on the long-term (pre-Quaternary) evolution of strike-slip faulting and nature of tectonic deformation in the DF region are available only to the south of the study area, along the E-W Kuh-Faghan Fault (Figures 1 and 2). There, a polyphase Miocene to Quaternary tectonic evolution is documented, involving the nucleation and propagation of intracontinental dextral shearing (Calzolari, Della Seta, et al., 2016; Calzolari, Rossetti, et al., 2016). In particular, thermochronological data document spatially and temporally punctuated fault system evolution that well fits into the two-stage early Miocene collision-enhanced and the late Miocene to early Pliocene tectonic reorganization of the Iranian region (Calzolari, Della Seta, et al., 2016).

The existing information on the paleostress regimes in the DF region is available from the fault slip analysis presented in Farbod et al. (2011), which documents a progressive transition of the horizontal maximum compression direction (σ_1) from an early NW-SE and N-S orientation to a NE-SW one that controls the modern state of stress. A post-Miocene transition from NW-SE to NNE directed maximum compression direction is also derived from the analysis of the Cenozoic folding to the west of the study area (Javadi et al., 2013) (Figure 1). The stress solution as obtained from inversion of focal mechanism solutions (Shabanian et al., 2010; Zamani et al., 2008) and geodetic measurements (Mousavi et al., 2013; Zarifi et al., 2013) across and to the north of the DF region has documented a seismotectonic scenario dominated by a NNE trending σ_1.

3.1. The Study Area

The study area is located to the north of the active trace of the central segment of the DF, from longitude 58°E to 59°E (Figures 2 and 3). The geology of the study area is dominated by the exposure of the calc-alkaline Eocene Kashmar granitoids (Shafaii Moghadam et al., 2015; Soltani, 2000), which defines an approximately 100 km long magmatic belt (hereafter referred as Kashmar-Azghand Intrusive complex, KAIC) to the north of the Kashmar and Azghand cities (Figure 3). The U-Pb zircon dating of the southern rim of the KAIC provided a middle Eocene (40–41 Ma) age (Shafaii Moghadam et al., 2015). The granitoids are emplaced within a thick pile of Paleocene-Eocene, Nummulite-bearing volcanoclastic successions (Shafaii Moghadam et al., 2015; Soltani, 2000; Taheri et al., 1998) that unconformably overlie discontinuous Mesozoic (Jurassic and Cretaceous) sedimentary and Precambrian and Paleozoic basement units, which are exposed along NE-SW, fault-bounded structural highs in the western sector of the study area (Figure 3). This structural setting is interpreted as the consequence of a Cretaceous-Paleocene tectonic inversion of the pristine horst and graben structures formed during a Mesozoic rifting phase (Taheri et al., 1998). These units are unconformably overlain by a ~2 km thick succession of reddish continental conglomerates and sandstones, known as the Oligocene Lower Red Fm (Behroozi et al., 1987; Eftekhar-Nezhad et al., 1976; Farbod et al., 2011, 2016). Despite original contacts having been reworked by faulting, a major erosional unconformity can be recognized between the KAIC and the basal deposits of the Lower Red Fm, which also contain boulders (up to 1 m in diameter) of the Eocene granitoids (Figure 4). This field evidence indicates that the KAIC was already exhumed and exposed to erosion prior of the sedimentation of the Lower Red Fm.

Discontinuous continental deposits of the Miocene Upper Red Fm crop out in the southern sector of the study area, where they are systematically observed in fault contact with those of the Lower Red Fm (Behroozi et al., 1987; Farbod et al., 2011, 2016) (Figure 3). Quaternary continental deposits, consisting of gray unconsolidated conglomerates and gravels, unconformably cover the previously described units and are commonly involved in faulting (Taheri et al., 1998; Fattahi et al., 2007; Farbod et al., 2011, 2016).

The seismotectonic scenario of the study area is characterized by complex kinematics, varying from pure reverse to pure sinistral faulting, and fault segmentation (Farbod et al., 2011). The major seismogenic structures are observed to the north of the DF trace, corresponding to the NE-SW sinistral faults (Dahan-Qaleh and Taknar faults), and to the west of it, along the reverse, NW-SE striking, Kharturan Fault (Farbod et al., 2011, 2016; Fattahi et al., 2007; Pezzo et al., 2012) (Figure 2).

4. Materials and Methods

Brittle structural analysis and apatite thermochronology are combined in this study with the aim to link tectonic structures to the major episodes of rock exhumation/uplift, and hence to reconstruct the long-term evolution of the DF. The low-temperature closure of isotope systems in AFT (partial annealing zone (PAZ): 75–120°C, with an effective closure temperature of 110 ± 10°C; Green & Duddy, 1989; Ketcham et al., 1999)

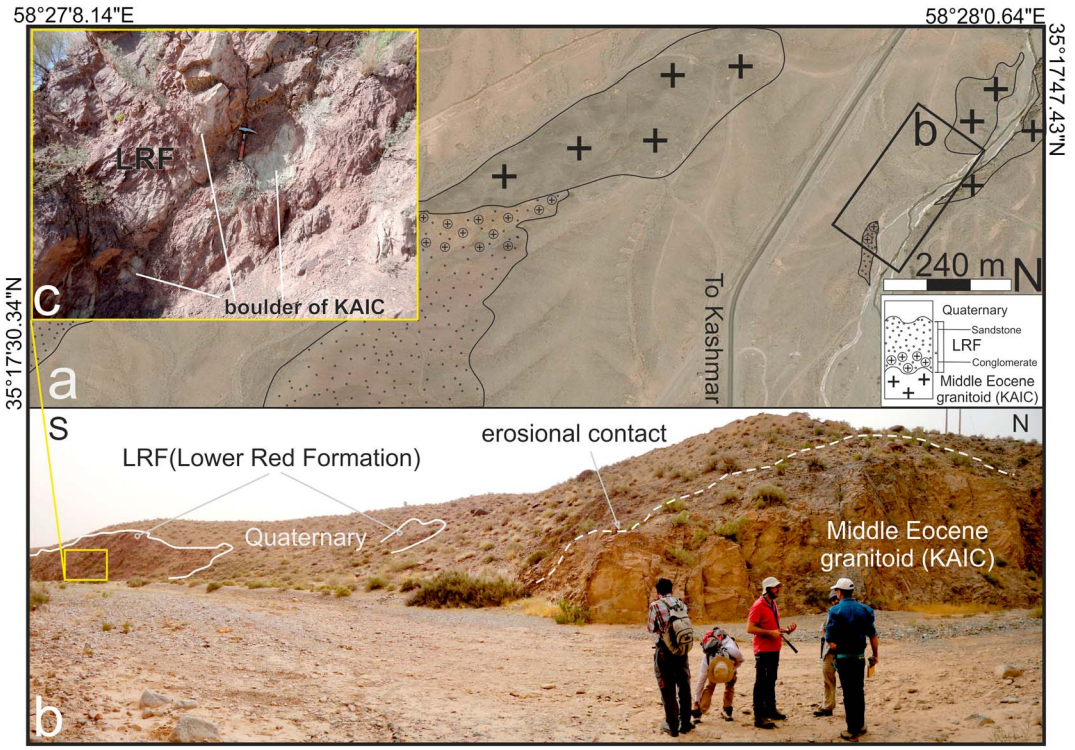

Figure 4. (a) Satellite image showing the stratigraphic relations between the middle Eocene KAIC and the overlying Oligocene Red Fm (LRF; see Figure 3 for location). (b) Panoramic view showing the erosional contact at the base of the Oligocene Lower Red Fm (see Figure 4a for location). (c) Enlargement (see Figure 4b for location) showing up to 1 m sized boulders derived from the KAIC within the Lower Red Fm.

and AHe (partial retention zone (PRZ): 40–80°C, with an effective closure temperature of 70 ± 10°C; Farley, 2000) makes this techniques particularly useful to assess the cooling history in the upper 3–5 km of the of the crust, where brittle deformation prevails.

Analyses were focused on the Eocene KAIC cropping out to the north of the trace of the active DF (Figure 3), since the granular (dominantly isotropic) igneous texture provides the opportunity to derive the regional paleostress directions from inversion of the fault slip data. Structural investigations were devoted to defining the structural architecture at regional scale by multiscale observations. Recognition and characterization of the brittle structural fabrics and description of fault patterns and their kinematics was mainly based on classical criteria as derived from the analysis of the striated fault surfaces (e.g., Doblas, 1998; Fossen, 2010; Petit, 1987), complemented by recognition of geological offsets in the field and as derived from remote sensing analysis. Structural data on faults, joints, veins, and bedding were collected at 194 georeferenced field analysis sites distributed in the study area (see supporting information S1). A total of 1,052 (measured faults and associated slickenlines) data were collected. The fault population analysis and the inversion of the fault slip data implemented to obtain regional paleostress directions was performed using the computer program Daisy v522e (http://host.uniroma3.it/progetti/fralab/). By the use of a polymodal Gaussian distribution statistics (Storti et al., 2006) (see Appendix A for details on computation techniques), the collected fault population was separated in four main kinematic groups based on the measured pitch angle of the fault slickenlines (the angle on the fault plane measured clockwise from above between the fault strike and the slickenline, ranging 0–180°) as dextral, sinistral (pitch angle of the slickenlines: 0–30°, 150–180°), reverse, and extensional (pitch angle of the slickenlines: 70–120°). The stress inversion method based on the rotax (also known as "slip normal," i.e., the line lying on the fault surface and orthogonal to the slickenlines; Salvini et al., 1999; Storti et al., 2006; Wise & Vincent, 1965) analysis option enclosed in the Daisy v5.22e software (multiple-faulting method; see Appendix A for details on computation techniques) is adopted in this study. Rotax analysis is a standard practice to discriminate between polyphase faulting events (see, e.g.,

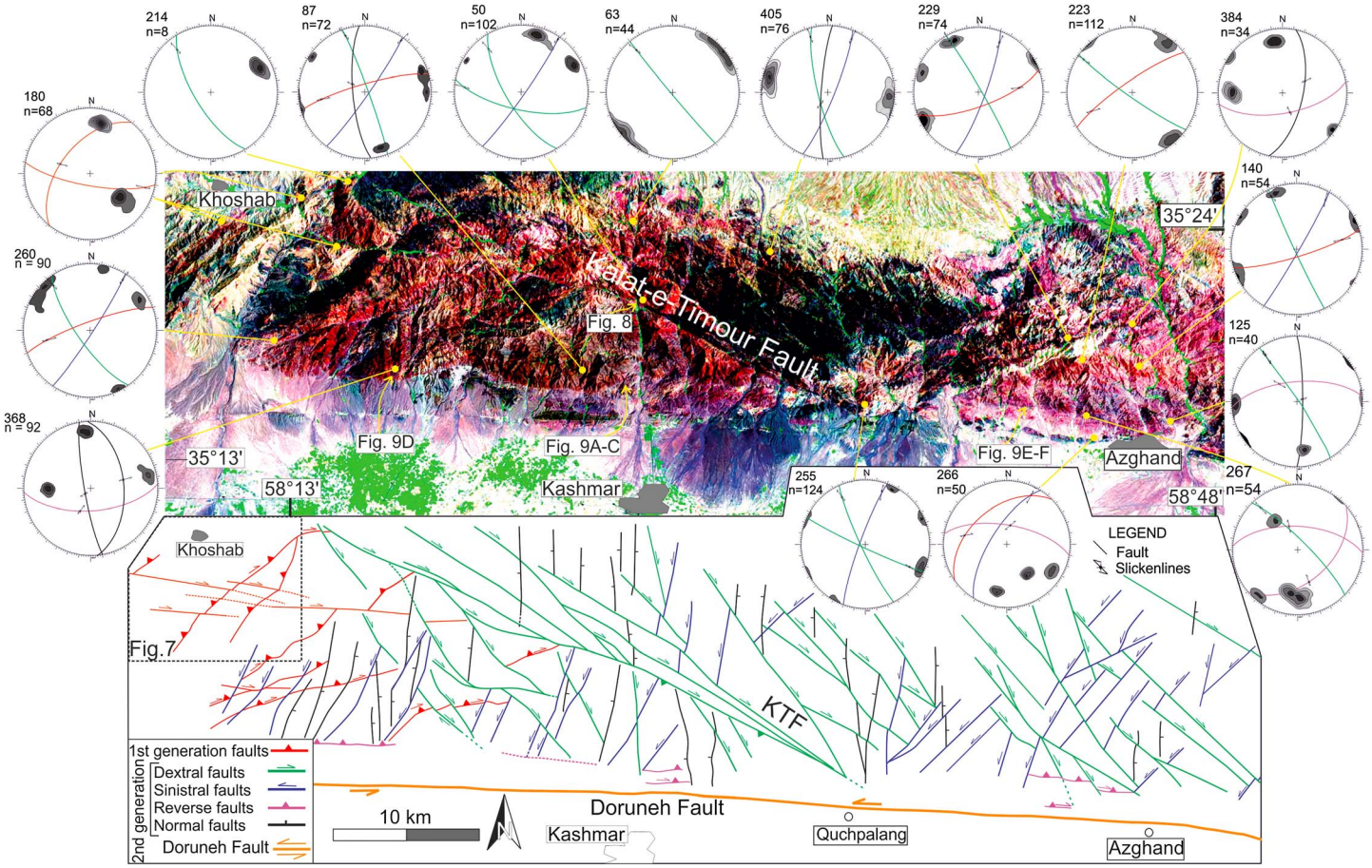

Figure 5. Multiresolution Seamless Image Database (MrSID) satellite image (top) of the study area and interpretative line drawing (down) showing the main fault systems with their kinematics indicated (see text for further details). Representative stereoplots (Schmidt net, lower hemisphere projection) showing the fault data set (see also the supporting information S2 for the complete structural data set), presented as contour diagrams of poles to fault planes (contouring interval 2%), great circles and slikenlines (arrows). Dashed rectangle shows location of Figure 7; locations of Figures 8 and 9 are also indicated.

Salvini et al., 1999; Storti et al., 2006; Tavani et al., 2011). In the assumption of dynamic rupture according to the Coulomb Failure criteria, the line on the fault plane normal to the slip vector (the fault rotax) lies parallel to the σ_2 direction. Statistical analysis of the rotax attitude distribution allows first to subdivide the fault populations into possible conjugate subsets and then to obtain the corresponding (paleo)stress directions (Salvini et al., 1999; Salvini & Vittori, 1982).

A total of 11 samples were collected from KAIC for AFT and AHe thermochronometry (see Appendix A for details on the analytical protocols adopted in this study) in order to link the paleostress reconstruction to the post-Eocene exhumation/burial history of the KAIC. All samples were collected along two altimetric profiles, located in the eastern and western sector, and hereafter referred as transect-1 (T-1) and transect-2 (T-2), respectively (see Figure 3 for location of the sampling transects). The apatite grains were separated by crushing, sieving, standard heavy liquid, and magnetic separation according to the procedure described in Appendix A.

5. Structural Architecture

The structural architecture of the study area is depicted in the structural map shown in Figure 5, where the major fault traces and relative kinematics are indicated (see also supporting information S2). The map is derived from the existing geological cartography at the 1:100.000 and 1:250.000 scale (Behroozi et al., 1987; Eftekhar-Nezhad et al., 1976; Taheri et al., 1998) and has been revised based on original field work, integrated with extensive remote sensing analysis using Landsat satellite and Google Earth imagery.

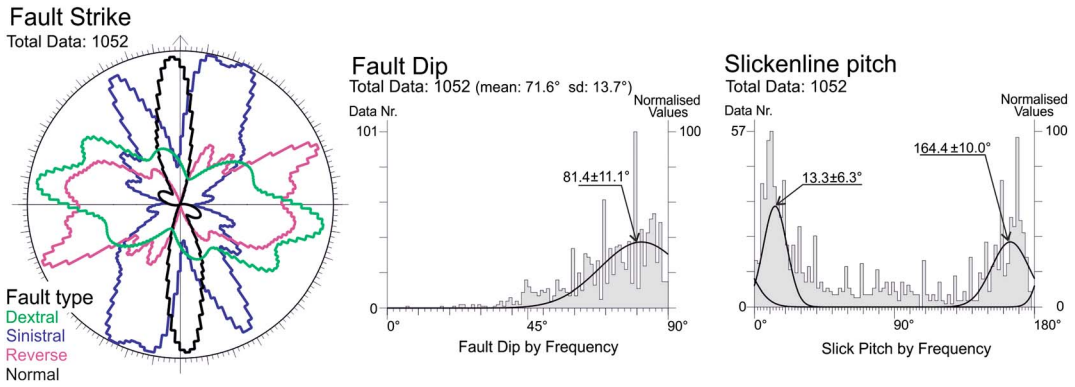

Figure 6. Left: Rose diagram of faults strike for the cumulative fault population. Right: Frequency and Gaussian best fit analysis of fault dip (left) and slickenline pitch angle (right) of the measured fault population.

An array of distributed, subvertical fault strands are recognized to cut across the Eocene KAIC and the host Paleogene volcano-sedimentary units exposed in the study area (Figures 3 and 5). The results of the polymodal Gaussian statistics (Storti et al., 2006) applied to the collected cumulative fault population (1052 data) are shown in Figure 6. Dextral faults show main strikes at N65°, N101°, and N156°, whereas the sinistral faults at N27°, N10° and N152°, respectively. For what concerns dip-slip faults, reverse faults exhibit main strikes at N68°, N103°, and N30°, extensional faults at N177° and N120°. The dominant strike-slip character of the regional faulting is attested by the mean pitch angle of the slickenlines, of 13° and 162° (Figure 6). The overprinting relationships among these different fault strands are clearly observable at regional scale and in the field (Figures 3 and 5), providing the evidence of a polyphase tectonic evolution as the result of two main generations of tectonic structures.

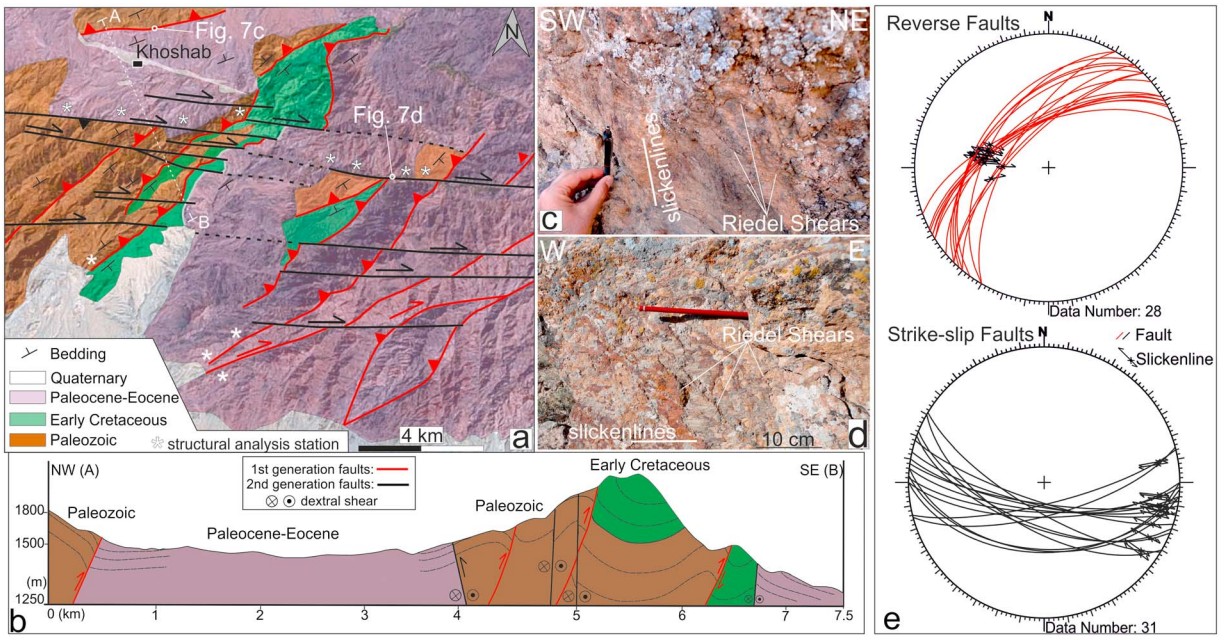

Figure 7. (a) Geological and structural map of the NW corner of the study area (Koshab area in Figure 5) on the shaded-relief SRTM. The white dashed line shows the trace (indicated as A-B) of the geological cross section shown in Figure 7b). (b) Interpretative geological cross section, showing the overprinting relationships between the first-generation NE-SW reverse and E-W dextral fault systems. (c) Example of a polished fault surface belonging to the NE-SW striking reverse fault systems (Permian carbonates). Slickenlines are nearly dip-parallel and kinematic indicators, as provided by synthetic Riedel shears and lunate fractures, indicate reverse kinematics. (d) Example of a polished fault surface part of the E-W striking dextral fault system (Paleocene-Eocene deposits). The slickenlines are strike parallel, and the kinematic indicators are provided by synthetic Riedel shears and lunate fractures, pointing to dextral shear. (e) Stereoplots (Schmidt net, lower hemisphere projection) of the collected fault data (fault as great circle and striae as arrows).

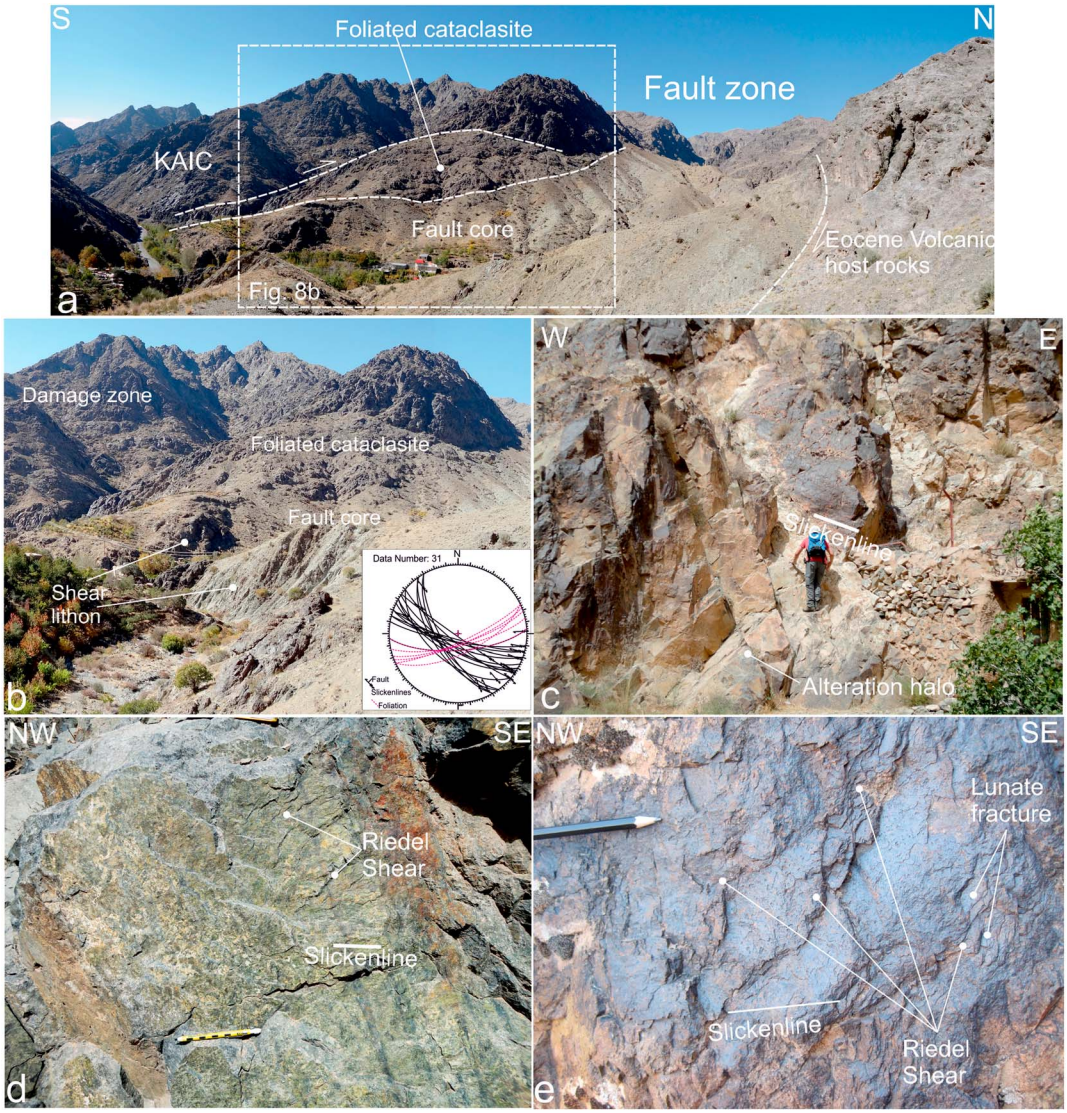

Figure 8. (a) Panoramic view showing the structural architecture of the dextral, NW-SE Kalat-e-Teimor fault (KTF in Figure 3) controlling the contact between the KAIC and the Eocene volcanic sequences (host rocks). (b) Close-up of the fault zone showing the fault damage zone and the fault core. The fault core mostly localizes within the host Eocene volcanics, with local development of foliated cataclasites. The stereoplot (Schmidt net, lower hemisphere projection) shows the corresponding structural data measured in the area (fault surfaces and secondary foliation as great circles and striae as arrows). (c) Meter-scale, NW-SE striking polished fault surfaces showing subhorizontal slickenlines and diffuse fault-controlled rock alteration in the KAIC (structural analysis site 50). (d, e) Mesoscale NW-SE striking polished fault surfaces in the KAIC, with subhorizontal slickenlines and kinematic indicators as provided by synthetic Riedel shears and lunate fractures indicating dextral kinematics. See Figure 5 for location of figures.

The first generation of tectonic structures is recognized on the north-western corner of the study area (Khoshab area), where the pre-Eocene sequences are exposed, and to the south of the Kalat-e-Teimor Fault (Figure 5). In the Khoshab area (Figure 7a, station 180 in Figure 5), high-angle NE-SW striking, NW dipping faults juxtapose folded Paleozoic (Permian limestones of the Jamal Fm) and Mesozoic (early Cretaceous Orbitolina-bearing limestones) cover rocks in the hanging wall onto Eocene, Nummulite-bearing deposits in the footwall (see the cross section in Figure 7b). Fault kinematics is dip-slip reverse with a minor dextral component (pitch angle of slickenlines: 70–75°; Figure 7c; see the stereoplot in Figure 7e, red fault planes) and the fault zones are marked by decameter-thick damage zones, mostly developed within the hanging wall rocks. These reverse faults are cut across by a set of steeply dipping dextral fault strands, roughly E-W

(N90–120°) striking (Figures 7a and 7b). The analysis of the fault kinematics documents nearly pure strike-slip motion (pitch angle of slickenlines: 5–17°; Figure 7d; see stereoplot in Figure 7e, black fault planes). There is stratigraphic evidence of fault offsets across these dextral faults, which are in the order of 1–2 km for the single fault strand (Figure 7a).

Moving toward the east, the first generation NE reverse and E-W dextral faults abut against the NW-SE Kalat-e-Teimur Fault that is part of the second generation of fault structures. This high-angle fault cuts obliquely across the KAIC and defines the major fault zone in the study area, reworking the original intrusive contacts and dying out toward the SE (Figure 3). The fault damage zone is more than 300 m thick and it is made up of a verticalized panel of highly fractured rocks. The fault core is defined by a approximately 50–100 m thick gouge, mostly developed in the volcanic host rocks and dipping steeply to the SSW (Figures 8a and 8b). Fault data document a dominant strike-slip motion with a minor component of dip-slip (reverse) motion (pitch angle of slickenlines: 5–21° and 140–172°; see stereoplot for station 50 in Figure 5; Figures 8c and 8d). The phyllonite fault rocks exhibit a penetrative S-C fabric made up of WSW-ENE striking tectonic foliation and NW-SE slip surfaces (see the stereoplot in Figure 8b). Fault kinematics as deduced from kinematic indicators on polished fault surfaces, including Riedel shears, lunate fractures, ridge-in-groove lineations, and S-C fabrics, systematically point to dextral kinematics (Figures 8b and 8e).

The fault pattern within the KAIC is distinctly different in the northern and southern fault blocks delimited by the Kalat-e-Teimur Fault (Figure 5). In the southern block, the first generation of fault structures are well preserved and made of a set of subvertical NE-SW striking dextral transpressive to reverse fault strands, mostly localized along the boundary between the KAIC and the host volcanic rocks (see stereoplots for station 180 and 260 in Figure 5). These faults are cut across by a complex array of second-generation faults, made of NNW-SSE dextral (striking N140–170°), NNE-SSW sinistral (N10–30°), and nearly NS striking (N170°–N10) extensional (see stereoplots for station 223, 229, and 405 in Figure 5) fault strands. In the northern block, the structural architecture is instead controlled exclusively by the second generation of faults that consist of conjugate arrays of NNW-SSE dextral and NNE-sinistral fault strands (see stereoplots 50, 87, 140, 229, 255, and 405 in Figure 5), associated with N-S striking extensional faults (Figures 5, 9a, and 9d). These fault strands are closely spaced (at about 0.5 1 km intervals), with mutual cross-cutting relationships (Figure 5) As recognized both at the outcrop (Figure 9a) and regional scale (Figure 5), the acute dihedral angles defined by the conjugate strike-slip faults are commonly bisected by N-S striking veins/fractures and extensional faults (see stereplots 87 and 368, 384, and 405 in Figures 5, 9a, and 9b). The major deformation zones are usually characterized by dm-thick damage zones, and on polished fault surfaces, the kinematic criteria are dominantly provided by Riedel shears, lunate fractures, and ridge-in-groove lineations (Figure 9c). The extensional faults also commonly form conjugate arrays (Figure 9d), often in association with subparallel fractures and veins. At the southward termination of the KAIC, a set of ENE-WSW to E-W striking, northward dipping reverse faults control the tectonic contacts between the KAIC with the Eocene volcanoclastic host rocks and, locally, of these latter deposits with the Oligocene sediments of the Lower Red Fm (see stereoplot 125, 225, 266, 267, and 368 in Figure 5). Within the KAIC, these faults are associated with development of up to 0.5 m thick fault cores, with the local development of foliated cataclasites (Figures 9e and 9f).

To sum up, a first generation of NE-SW reverse-to-dextral transpressive faults associated with roughly E-W striking dextral ones is overprinted by a second generation of faults that comprise a set of conjugate strike-slip faults, (N)NW (dextral) and (N)NE (sinistral), in association with N-S extensional and E-W reverse faults. Mutual cross-cutting relationships are recognized among the second generation of fault strands in the study area (Figure 5).

6. Thermochronology

6.1. AFT Results

Only 7 out of 11 granitoid samples collected from the Eocene KAIC provided AFT measurements. Specifically, two samples are from the T-1 (F2-09 and F2-12) and five samples are from T-2 (I13-06, F2-04, F2-05, F2-07, and F2-08).

Results of the AFT analysis are presented in Table 1. The AFT ages span from 60.8 ± 9.2 to 15.4 ± 2 Ma, showing a poor correlation with the sample elevation (Figure 10a). The majority of the AFT samples (5 out of 7)

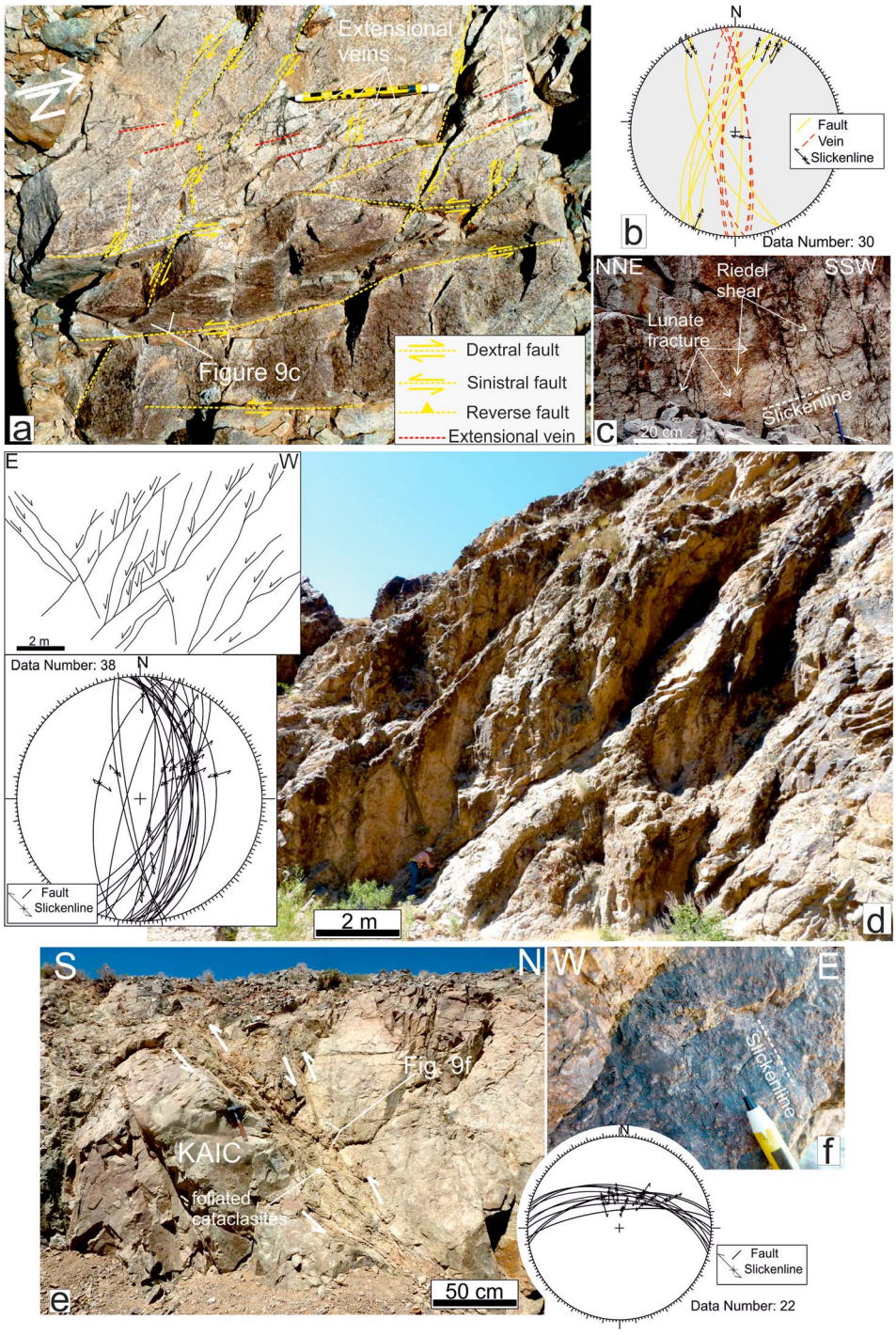

Figure 9. (a) Outcrop-scale conjugate arrays of NNW-SSE dextral and NNE-SSW sinistral faults cutting across the KAIC. Note the N-S striking veins and fracture arrays that bisect the acute dihedral angles defined by the conjugate faults. (b) Stereoplot (Schmidt net, lower hemisphere projection) showing the collected structural data. (c) Close-up of a fault surface (see Figure 9a) showing subhorizontal slickenlines and kinematic indicators as provided by Riedel shears and lunate fractures pointing to sinistral shear. (d) N-S striking conjugate normal fault systems cutting across the Eocene volcanic units (structural analysis site 368) and interpretative line drawing (top left). The stereoplot (Schmidt net, lower hemisphere projection) shows the corresponding fault data (fault as great circle and striae as arrows). (e) E-W striking, N dipping reverse faults at the southern termination of the KAIC. Foliated cataclasites decorate the fault core. The stereoplot (Schmidt net, lower hemisphere projection) shows the collected structural data. (f) Detail (see Figure 9e) showing a close-up of a fault surface showing dip-parallel slickenlines and kinematic indicators as provided by Riedel shears and lunate fractures pointing to reverse shear. See Figure 5 for location of figures.

Table 1
List of the Studied Samples for AFT Thermochronology, With Geographical Location and Results of the AFT Measurements Indicated

Sample number	Location (latitude-longitude)	Elevation (m)	Number of crystals	Spontaneous track density (×10 cm^2)	Induced track density (×10 cm^2)	Confined track (mean length ± SD; μm)	Dpar (mean ± SD; μm)	AFT age ± σ (Ma)	Chi-square (c^2) test	P (c^2) %
I13-06	58°28′0.50″E–35°19′13.70″N	1,283	20	1.80	12.43			25.8 ± 2.7	2.80	100.00
F2-04	58°27′33.22″E–35°19′42.55″N	1,375	20	1.54	17.86	12.16 ± 1.47	1.36 ± 0.11	15.4 ± 2	2.38	100.00
F2-05	58°27′4.12″E–35°19′59.69″N	1,523	20	3.42	10.60	12.35 ± 1.18	1.37 ± 0.12	55.7 ± 5.7	20.16	38.50
F2-07	58°26′9.27″E–35°20′29.49″N	1,813	20	1.82	5.08			60.8 ± 9.2	1.38	100.00
F2-08	58°26′15.13″E–35°20′33.45″N	1,887	8	1.04	3.41			57.3 ± 11.6	0.67	100.00
F2-09	58°46′55.90″E–35°17′31.98″N	1,384	15	2.38	7.23			55.7 ± 6.6	7.86	98.80
F2-12	58°46′20.50″E–35°19′1.42″N	1,876	20	1.46	5.57			49.2 ± 7.8	0.31	100.00

Note. All calculation were computed with a Zeta number of 362.48 ± 12.69.

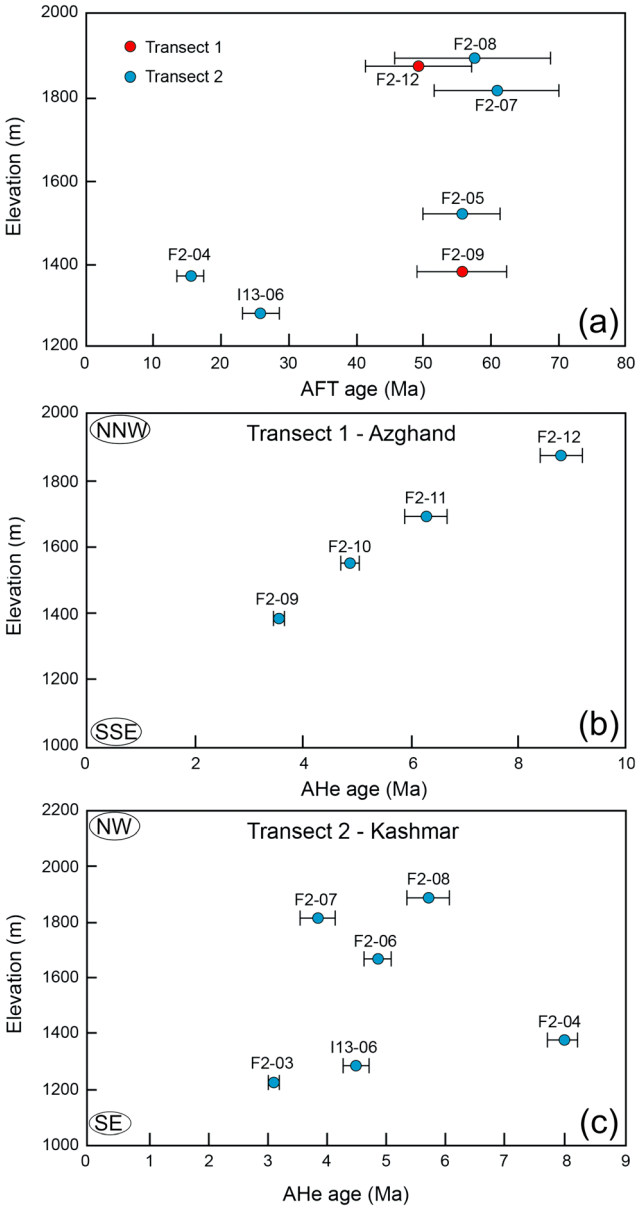

Figure 10. (a) AFT age versus elevation graph. (b) AHe age versus elevation graph for sampling Transect-1. (c) AHe age versus elevation graph for the sampling Transect-2 (see Table 2 for further details).

provide Paleocene-early Eocene ages (from 60.8 ± 9.2 to 49.2 ± 7.8 Ma); only two samples show Oligocene (25.8 ± 2.7 Ma; sample I13-06) and middle Miocene (15.4 ± 2 Ma; sample F2-04) ages. Consequently, only the latter samples show AFT ages younger than the independently obtained Middle Eocene U-Pb zircon crystallization age (approximately 40–41 Ma; Shafaii Moghadam et al., 2015). Radial plots as obtained through the TrackKey 4.2 software (Dunkl, 2002) are shown in Figure 11a, where the U-Pb zircon age of the KAIC at 41 Ma and the inferred age of the erosional unconformity at the base of the Lower Red Fm, here placed at 34–31 Ma (Morley et al., 2009; Rezaeian et al., 2012), are also shown. These plots show that sample F2-04 is fully reset and sample I13-06 almost fully reset by the burial phase associated with deposition of the Lower Red Fm. A significant number of confined track length measurements were obtained for samples F2-04 and F2-05 (Table 1 and Figure 11b). Confined track lengths for both samples show an unimodal distribution, with peaks at 14.7 μm and at 14.4 μm for samples F2-04 and F2-05, respectively, suggesting rapid cooling (Galbraith & Laslett, 1993) (despite having occurred in different times). The etch pit diameter, Dpar, for AFT F2-04 and F2-05 which are within the 0.94–1.57 and 1.16–1.7 interval, respectively, was used to infer annealing kinetics (Burtner et al., 1994). Dpars for both samples are in the range of standard Durango apatite (Ketcham et al., 2007).

6.2. AHe Results

Up to three single-grain aliquots were dated for each sample, as shown in Table 2. The quality of AHe results was checked using criteria such as value of U, Th and He and their relative errors, possible relationships between age and eU or radius and inconsistencies between the AHe and AFT ages. Analytical data are in general acceptable, although critically low He and U concentrations (<1 mol/g and <10 ppm) occur in some grains. In cases of low reproducibility, this is mostly due to interplay of several factors (e.g., fractures, crystal defects, and impurities) given that the dated grains were generally far from ideal. The scarce correlation between age and compositional parameters suggests that the effects of zonation, inclusions, and coating are not significant. Samples with reproducible ages therefore indicate a minor effect of bad crystal features and their weighted mean can be used for interpretation.

The AHe ages range from 12.7 ± 0.6 to 2.8 ± 0.1 Ma. In particular, results derived from the eastern T-1 show a southward decrease in mean age

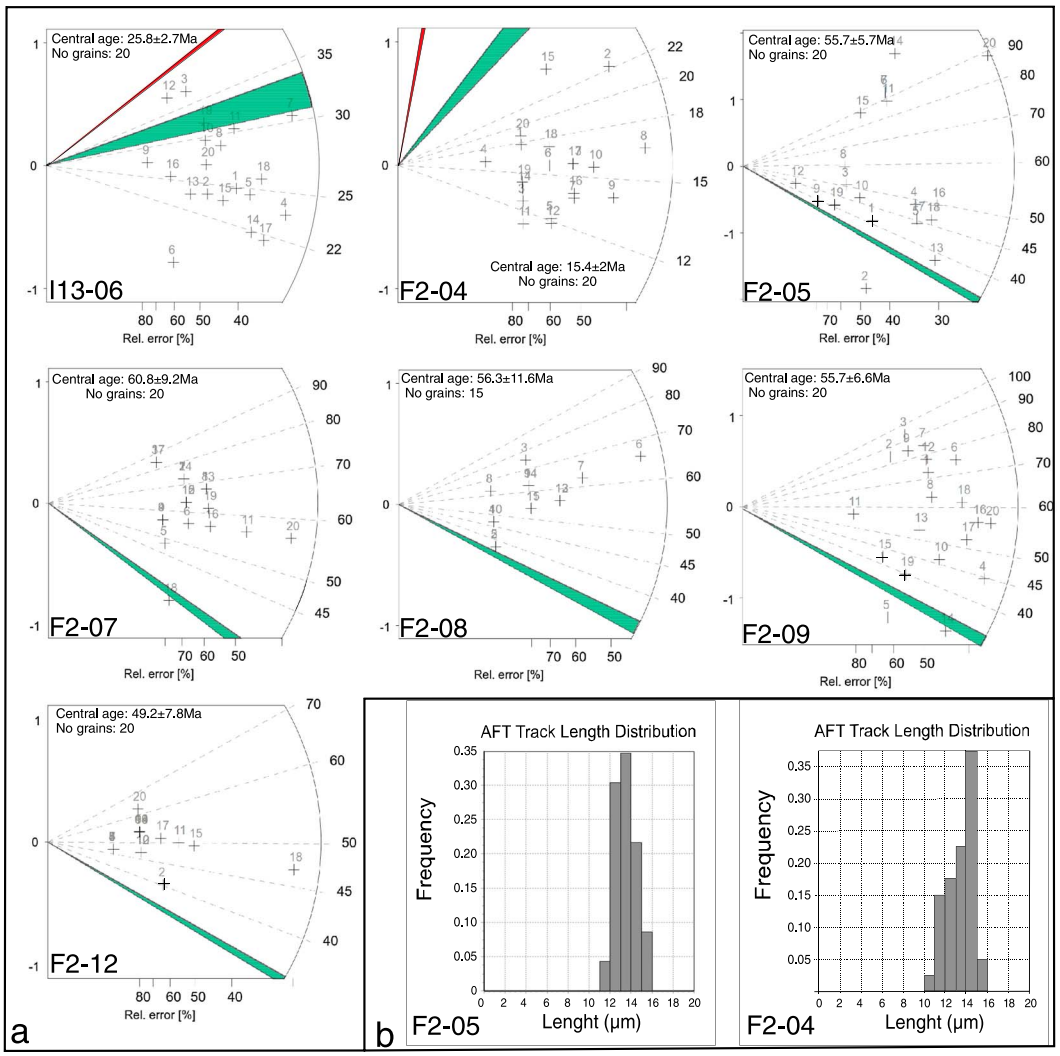

Figure 11. (a) Radial plots for AFT samples with formation ages (red areas) and the Eocene-Oligocene boundary unconformity age (green areas) indicated. Central age, relative error, and number of grains are provided in each plot. (b) AFT confined track length distribution for the two measured samples. Radial plots were constructed using the TRACKKEY 4.2 software (Dunkl, 2002).

from 8.8 to 3.5 Ma that readily correlates with a decrease in sample elevation (Figure 10b). This elevation-age relationship suggests the granitic body exhumed as a coherent block from approximately 8.8 Ma to 3.5 Ma. The western sampling transect-2 provides AHe mean ages ranging from 8.0 ± 0.26 to 3.1 ± 0.1 Ma. The AHe ages versus elevation diagram for this transect shows a poor correlation, such as the southward age rejuvenation (Figure 10c).

In summary, the results of the AFT and AHe thermochronology indicate the KAIC cannot be regarded as a homogeneous magmatic body. In particular, our AFT data (Figure 3) suggest that it consists of composite, chronologically distinct magma batches, likely Paleocene-Eocene in age. Furthermore, the markedly different distribution of the AFT ages within the KAIC (see also Figure 10a) suggests that only locally (southern sector of the KAIC; see Figure 3) the AFT system was reset, whereas the AHe system was fully reset.

6.3. Time-Temperature Modeling

In order to reconstruct the low-temperature (in the range ~130–45°C) cooling history (*T-t*) of the study area, AFT and AHe data from the KAIC were modeled through the HeFTy software (Ketcham, 2005). HeFTyY software uses the Monte Carlo method to find the *T-t* paths compatible with observed AFT and AHe data such

Table 2
List of the Studied Samples for AHe Thermochronology, With Geographical Location and Analytical Data for the Single Apatite Grains Indicated

Sample number	Location (latitude-longitude)	Elevation (m)	Radius (μm)	U (ppm)	Th (ppm)	^{4}He (nmol/g)	eU (ppm)	Corrected single crystal AHe age ± σ (ma)	Weighted mean AHe age ± σ (ma)
F2_03_1	58°27′58.26″E–35°18′38.39″N	1225	58.91	39.47	11.28	0.50	42.12	2.87 ± 0.16	
F2_03_2	58°27′58.26″E–35°18′38.39″N	1225	48.56	60.63	145.42	1.26	94.80	3.53 ± 0.22	3.11 ± 0.1
F2_03_3	58°27′58.26″E–35°18′38.39″N	1225	50.22	30.39	9.58	0.40	32.64	3.1 ± 0.13	
I13_06_1	58°28′0.50″E–35°19′13.70″N	1283	85.87	29.44	36.60	0.54	38.04	3.17 ± 0.15	
I13_06_2	58°28′0.50″E–35°19′13.70″N	1283	61.77	36.68	37.39	1.10	45.47	5.82 ± 0.27	4.5 ± 0.21
F2_04_1	58°27′33.22″E–35°19′42.55″N	1375	36.71	15.46	33.36	0.64	23.30	8.15 ± 0.42	
F2_04_2	58°27′33.22″E–35°19′42.55″N	1375	55.30	37.22	53.20	1.31	49.72	6.53 ± 0.44	7.99 ± 0.26
F2_04_3	58°27′33.22″E–35°19′42.55″N	1375	42.21	74.99	85.55	3.27	95.10	9.53 ± 0.48	
F2_06_2	58°26′41.32″E–35°20′13.66″N	1669	50.20	25.34	29.33	0.63	32.24	5.03 ± 0.26	4.87 ± 0.26
F2_06_3	58°26′41.32″E–35°20′13.66″N	1669	58.77	26.14	42.89	0.70	36.22	4.7 ± 0.27	
F2_07_1	58°26′9.27″E–35°20′29.49″N	1813	52.31	8.64	17.38	0.23	12.73	4.42 ± 0.27	3.84 ± 0.2
F2_07_3	58°26′9.27″E–35°20′29.49″N	1813	47.10	12.75	29.00	0.24	19.57	3.25 ± 0.34	
F2_08_1	58°26′15.13″E35–33.45″N	1887	44.03	8.31	23.54	0.36	13.84	6.92 ± 0.42	5.71 ± 0.34
F2_08_3	58°26′15.13″E–35°20′33.45″N	1887	43.21	9.13	22.97	0.24	14.53	4.5 ± 0.28	
F2_09_1	58°46′55.90″E–35°17′31.98″N	1384	70.46	9.50	21.69	0.24	14.60	3.7 ± 0.21	
F2_09_2	58°46′55.90″E–35°17′31.98″N	1384	58.45	12.58	25.65	0.25	18.61	3.23 ± 0.19	3.54 ± 0.1
F2_09_3	58°46′55.90″E–35°17′31.98″N	1384	49.03	19.55	48.22	0.43	30.88	3.65 ± 0.15	
F2_10_2	58°46′16.73″E35°18′23.81″N	1550	39.93	22.38	31.09	0.50	29.68	4.75 ± 0.28	4.86 ± 0.18
F2_10_3	58°46′16.73″E–35°18′23.81″N	1550	47.72	12.95	25.43	0.36	18.92	4.94 ± 0.23	
F2_11_1	58°46′21.49″E–35°18′50.28″N	1691	39.63	14.40	25.00	0.35	20.28	4.87 ± 0.4	
F2_11_2	58°46′21.49″E–35°18′50.28″N	1691	50.54	6.75	20.32	0.35	11.53	7.7 ± 0.36	6.29 ± 0.38
F2_12_2	58°46′20.50″E–35°19′1.42″N	1876	43.64	10.87	19.53	0.51	15.45	8.81 ± 0.39	8.81 ± 0.39

as spontaneous, induced tracks and confined tracks, apatite crystal dimension, amount of Uranium, Thorium and measured age. We decided to model only sample F2-04 as it is located close to the sites where U-Pb zircon formation ages are available (Shafaii Moghadam et al., 2015) and a significant number of tracks were measured.

The following independent constraints are adopted in the modeling (Figure 12): (i) the formation age of the KAIC is placed at 41 Ma after Shafaii Moghadam et al. (2015) (Box 1); (ii) the age of the erosional unconformity at the base of the Oligocene Lower Red Formation is placed at the Eocene-Oligocene boundary (see also Rezaeian et al., 2012; Box 2); and (iii) the present-day mean temperature is assumed at 15 ± 5°C. Based on the older AFT ages shown in the radial plots for the reset samples (samples F2-04 and I1306; Figure 11), resetting for the AFT system is placed at 20–28 Ma (Box 3; Figure 12).

From the output of the thermal modeling, four main stages are recognized (Figure 12). The first stage corresponds to an episode of enhanced cooling (~20°C/km) after crystallization and emplacement of the KAIC at the Eocene-Oligocene boundary, when KAIC was exhumed to the surface and eroded. The second stage is characterized by reheating, consistent with a burial phase to temperatures above the PAZ during the Oligocene. The third stage corresponds to exhumation-related cooling (approximately 10°C/km) during the early Miocene (22–18 Ma) after burial, followed by a steady state cooling at a much lower rate (approximately 1°C/km) up to the late Miocene. The fourth stage corresponds to a renewed episode of enhanced cooling (>10°C/km) starting at the Miocene-Pliocene transition, at about 5–6 Ma, during which the KAIC was finally exposed to the surface (Figure 12).

7. Discussion

The integration of the structural and low-temperature thermochronology data collected within the KAIC documents a prolonged record of intracontinental tectonics in the region to the north of the active trace of the DF during the Cenozoic (post-Eocene) times. Based on the fault cross-cutting relationships observed at the outcrop and regional scale, which attest for conjugate (N)NW-(S)SE dextral and (N)NE-(S)SW sinistral faults that overprint early NE-SW dextral transpressional and E-W dextral faults (Figures 3 and 5), a polyphase brittle tectonic evolution is recognized in post-Eocene times.

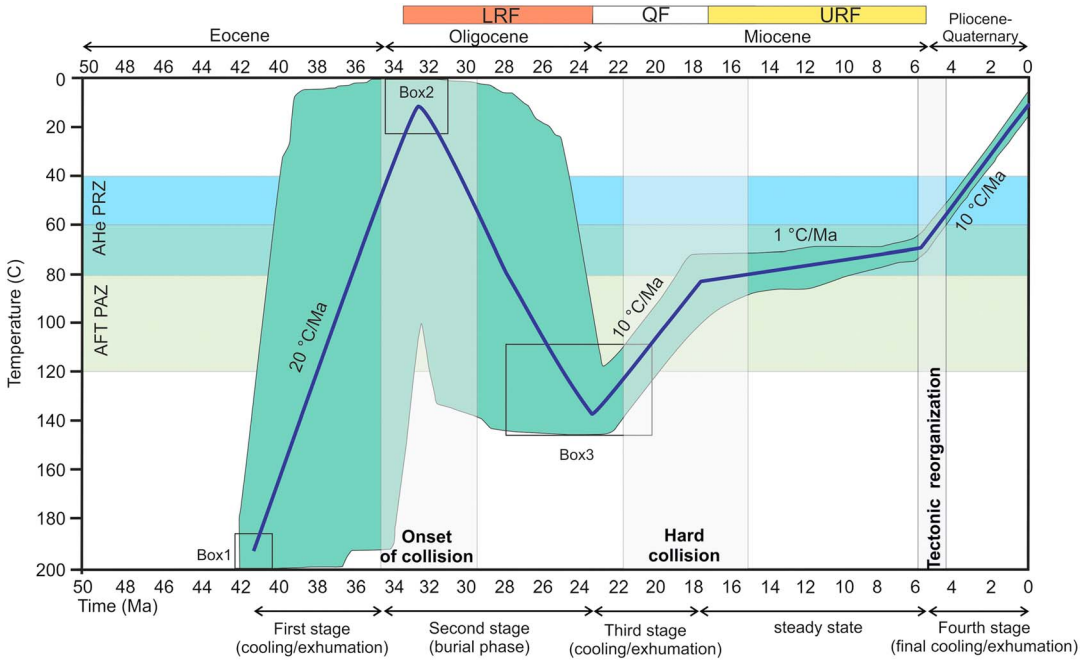

Figure 12. The *T-t* history of the KAIC as provided by the thermal modeling performed with the HeFTy software (Ketcham, 2005). The boxes indicate the *T-t* constraints adopted in this study, which refer to (i) the formation age of the KAIC that is placed at ~41 Ma (Shafaii Moghadam et al., 2015) (Box 1), (ii) the age of the unconformity at the base of the Lower Red Fm., placed at the Eocene-Oligocene boundary (Box 2), and (iii) the resetting for the AFT system that is placed at 28–20 Ma at 140°C (Box 3). The green area indicates the acceptable probability solutions and the blue line refers to the weighted-mean thermal history path. The stratigraphic ages of the Lower Red Fm (LRF), Qom Fm (QF), and Upper Red Fm (URF) are after Morley et al. (2009) and Rezaeian et al. (2012). The main regional tectonic events are also indicated (see text for further details).

7.1. Structural Evolution

In order to reconstruct the regional paleostress directions responsible for the reconstructed structural evolution, we first performed the frequency distribution analysis of the fault rotax population as derived from the cumulative fault slip data collected within the KAIC. This analysis reveals a well-defined, near-vertical cluster (mean orientation: 217°, 77°; Figure 13a), attesting to a (paleo-) σ_2 direction remained nearly vertical throughout the polyphase brittle tectonic evolution documented in this study and hence for a tectonic environment dominated by polyphase regional-scale strike-slip faulting/tectonics. In the assumption of fault-parallel simple shear conditions within the fault damage zone, the rotax analysis allows to discriminate among the different conjugate systems (synthetic R shears and antithetic R′ shears, respectively), which have a Coulomb relationship to one another and are oriented obliquely (at ± ~15° and ± ~75°, respectively) to the trace of the principal displacement zone (PDZ) (e.g., Davis et al., 1999; Mandl, 2000; Sylvester, 1988; Tchalenko, 1968) (Figure 13b). When applied to the cumulative strike-slip fault population (862 data over the total of 1052), three main conjugate subsets are recognized (total data: 635, corresponding to the 74% of the analyzed cumulative strike-slip fault population; Figure 13b and supporting information S3): (i) subset 1 (a and b), with mean strike of N94° (dextral) and N150° (sinistral); (ii) subset 2 (a and b), with mean strikes of N119° (dextral) and N06° (sinistral); and (iii) subset 3 (a and b), with mean strikes of N148° (dextral) and N28° (sinistral), respectively.

These subsets are compatible with a dextral PDZ oriented approximately ENE-WSW to E-W (for subset 1 and subset 2) and NW-SE for the subset 3 (Figure 13b), respectively, in good agreement with the field evidence (Figure 5). The corresponding paleostress solutions exhibit three main groups of paleo-σ_1 directions (trend and dip): (i) NW-SE (N301°, 02°) for subset 1, (ii) NNW-SSE (N335°, 6°) for subset 2; and (iii) ~NS (N182°, 17°) for subset 3, respectively. Collectively, these paleostress solutions point to two main groups of paleo-σ_1 directions, trending (N)NW-(S)SE and N-S, respectively (Figure 13b). These results are in accordance with the first-phase (assumed as Eocene in age) NW-SE directed regional shortening event proposed by Javadi

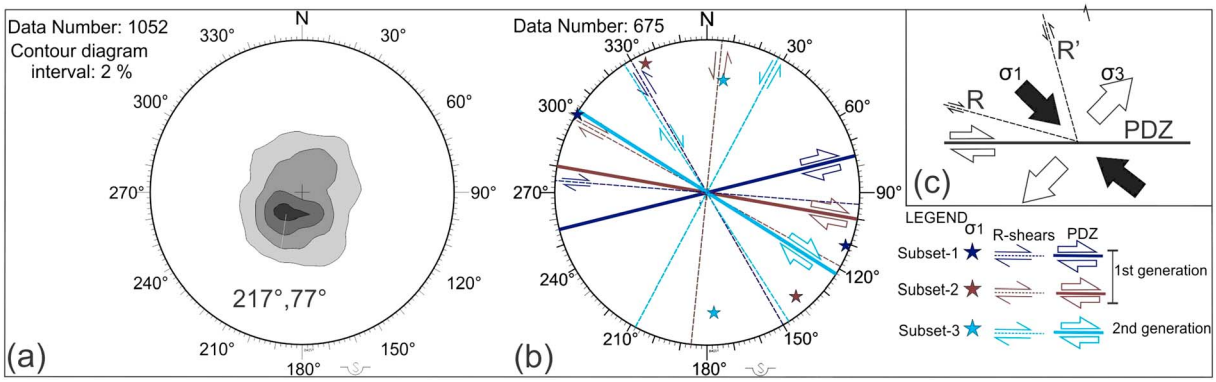

Figure 13. Results of the stress inversion as obtained through the Daisy software using the rotax analysis applied to the cumulative strike-slip fault slip data (see text and Appendix A for further details). (a) Contour diagram of the fault rotaxes (Schmidt net, lower hemisphere projection). (b) Stereoplot (Schmidt net, lower hemisphere projection) showing the mean fault strikes as derived from contour diagrams of poles to fault planes for the different conjugate Riedel subsets and the corresponding paleostress tensors (see text for further details).

et al. (2013) and with the paleostress states as reconstructed in Farbod et al. (2011), where NW-SE and N-S directed paleo-σ_1 directions are proposed.

Despite the fact that the assumptions made above may oversimplify the actual fault pattern evolution and the paleostress regimes in the study area, this reconstruction is compatible with and confirms the occurrence in the field of (i) the first generation of NE-SW reverse to dextral oblique faults (i.e., nearly orthogonal to the early NW-SE σ_1 direction), recognized in the western part of the study area, where they mainly correspond to reactivated preexisting (Mesozoic in age) rift-related structures (Figure 3); and (ii) the occurrence of roughly E-W reverse and N-S extensional faults (orthogonal and parallel to the subsequent N-S σ_1 direction, respectively), associated with the second-generation conjugate NNW-SSW dextral and NNE-SSW sinistral faults within the KAIC (Figures 3 and 5).

According to the reconstructed relative fault chronology (Figure 5), these results suggest a progressive clockwise rotation of the paleoregional stress field, resulting in the shift of the paleo-σ_1 direction from a ~NW-SE to a ~NS direction. Such a shift has been already recognized to the north of the study area, along the Alborz-Kopeh Dagh Mountains, during the Neogene-Quaternary transition (Ballato et al., 2013; Javidfakhr et al., 2011; Shabanian et al., 2010, 2012) and interpreted as a transient state of stress that was prevailing sometimes before the active stress state (the NE trending compression) in the region (Farbod et al., 2011; Javidfakhr et al., 2011; Shabanian et al., 2010). Similarly, a post-Pliocene change to NS directed maximum compression direction was recognized in the Zagros belt (Navabpour et al., 2007). Combining this evidence with the thermochronology results presented in this study, documenting a renewed stage of enhanced exhumation starting at the Miocene-Pliocene boundary (at about 5–6 Ma), we then propose that the Miocene-Pliocene transition corresponds to a major shift in the paleo-σ_1 direction from NW-SE to ~N-S and that this subsequent stress regime was responsible for the brittle structural architecture of the DF region.

7.2. Tectonic Synthesis

The integration of the structural and thermochronological data set confirms the reconstruction presented in Javadi et al. (2013), indicating pre-Quaternary dextral kinematics for the deformation zone to the north of the active trace of the DF. In particular, the polyphase history of strike-slip tectonics documented in this study is associated with a punctuated history of fault-related cooling, burial, and exhumation that occurred during the late Eocene to early Oligocene, the Oligocene to early Miocene, and the Miocene to Pliocene boundary, respectively (Figure 12). This polyphase history fits well with both the Cenozoic stratigraphy of the study area (Figure 3) and, at larger scale, with the main regional tectono/stratigraphic events recorded along the Bitlis-Zagros convergence zone.

The early episode of cooling/exhumation at the Eocene-Oligocene boundary (first stage in Figure 12) is in good agreement with the regional thermochronological data set, commonly interpreted as the time of onset of the Arabia-Eurasia collision (Allen & Armstrong, 2008; Ballato et al., 2011; François et al., 2014; Hafkenscheid et al., 2006; Hessami et al., 2001; Homke et al., 2009, 2010; Madanipour et al., 2013; McQuarrie et al., 2003;

Mouthereau et al., 2012; Robertson et al., 2006; Vincent et al., 2007). This time lapse also corresponds to a major stage of intracontinental deformation resulting from positive inversion tectonics documented in the Iran region along the Alborz and Kopeh Dagh Mountains (Guest et al., 2007; Madanipour et al., 2013; Robert et al., 2014).

This early episode of exhumation is followed by a burial phase during the Oligocene (second stage in Figure 12). This period corresponds to a phase of tectonic quiescence and regional subsidence as documented in Central Iran (Morley et al., 2009). In the DF region, it was accompanied by the deposition of the detrital continental sediments of the Oligocene Lower Red Fm, whose thickness was only locally (southern sector of the KAIC; see Figure 3) sufficient to reset the AFT system in the KAIC. On the other hand, thickness of the Lower Red Fm was sufficient to totally reset the AHe system in the KAIC (Figure 3).

The second episode of cooling/exhumation occurred during the Miocene times, with enhanced exhumation during the early Miocene (22–18 Ma), followed by a nearly steady state cooling/exhumation during the middle to late Miocene (Figure 12). This thermal evolution during the Miocene is compatible with the absence of sedimentation of the Qom Fm (Oligocene-Miocene in age; (Reuter et al., 2009) and the deposition of the Miocene Upper Red Fm in the regions that surround the exhuming KAIC (Figure 3). This time lapse is also consistent with the "hard continental collision" period (Ballato et al., 2011) along the Zagros convergence zone (Figure 12) and also in agreement with (i) the closure of the Neotethys seaways along the Bitlis/Zagros collisional front (Okay et al., 2010), and (ii) the accelerated exhumation of the Talesh Mountains in the western Alborz (Madanipour et al., 2017). Within Central Iran, this timing corresponds to (i) the early Miocene activation of dextral shearing to the south of the study area along the Kuh-e-Faghan Fault (Calzolari, Della Seta, et al., 2016) and reactivation of the Kashmar-Kerman Tectonic Zone in Central Iran (Karagaranbafghi et al., 2012; Verdel et al., 2007) (Figure 1).

The third and final episode of accelerated cooling/exhumation occurred at the Miocene-Pliocene boundary, which is compatible with the tectonic reorganization of the Iranian territory at regional scale (e.g., Allen et al., 2011) (Figure 12). This event is also nearly synchronous with (i) a change in the mode of accommodation of Arabia-Eurasia convergence along the Zagros collisional zone (Authemayou et al., 2006; Hatzfeld et al., 2010); (ii) the oroclinal bending of the Alborz Range, starting as younger than 7.3 Ma (Cifelli et al., 2015; Mattei et al., 2017); and (iii) renewed activity of dextral shearing in Central Iran as documented along the NE-SW Kuh-Sarhangi and E-W Kuh-e-Faghan faults during Pliocene-Quaternary times (Calzolari, Della Seta, et al., 2016; Calzolari, Rossetti, et al., 2016; Nozaem et al., 2013) (Figure 1).

Collectively, our results suggest that the Zagros convergent zone and the different tectonic domains in its hinterland (Figure 1) were mechanically/tectonically coupled since the middle Eocene. Furthermore, the evidence of no significant tectonic rotation occurred for the DF region during the Cenozoic, as documented by (i) paleomagnetic investigations in Central Iran (Cifelli et al., 2015; Mattei et al., 2012, 2017); and (ii) the maintenance of the NE-SW oriented regional tectonic fabrics throughout the DF region and to the south of it in the Kuh-Saranghi/Kuh-e-Faghan shear belt (Calzolari, Della Seta, et al., 2016; Calzolari, Rossetti, et al., 2016; Javadi et al., 2013, 2015; Nozaem et al., 2013) (Figures 1 and 2) is against the rigid block rotation models (e.g., Javadi et al., 2013; Walker & Jackson, 2004) as the cause of the observed, post-Eocene polyphase tectonic evolution of the DF region.

Based on the above discussion, a new tectonic reconstruction is presented below, which frames the spatiotemporal deformation distribution in Central Iran, as the result of the varying stress field conditions generated along the Zagros convergence plate boundary and the accommodation styles of the generated residual stress(es) in its hinterland domains.

7.3. Evolutionary Scenario

At the onset of the Arabia-Eurasia collision, during the Eocene-Oligocene times, the nearly orthogonal (NE directed) convergence at the plate margin (Allen & Armstrong, 2008; McQuarrie et al., 2003; Navabpour et al., 2007) was accommodated by the along-strike transition from continent-continent collision along the Zagros convergent margin to oceanic subduction along the Makran subduction zone (e.g., Mouthereau et al., 2012; Regard et al., 2005). As a result, we expect an along-strike (southeastward) decrease in the amount of the residual stress transmitted to the intraplate domain, following a general reduction in plate coupling at the plate boundary. Convergence was then largely accommodated by crustal thickening

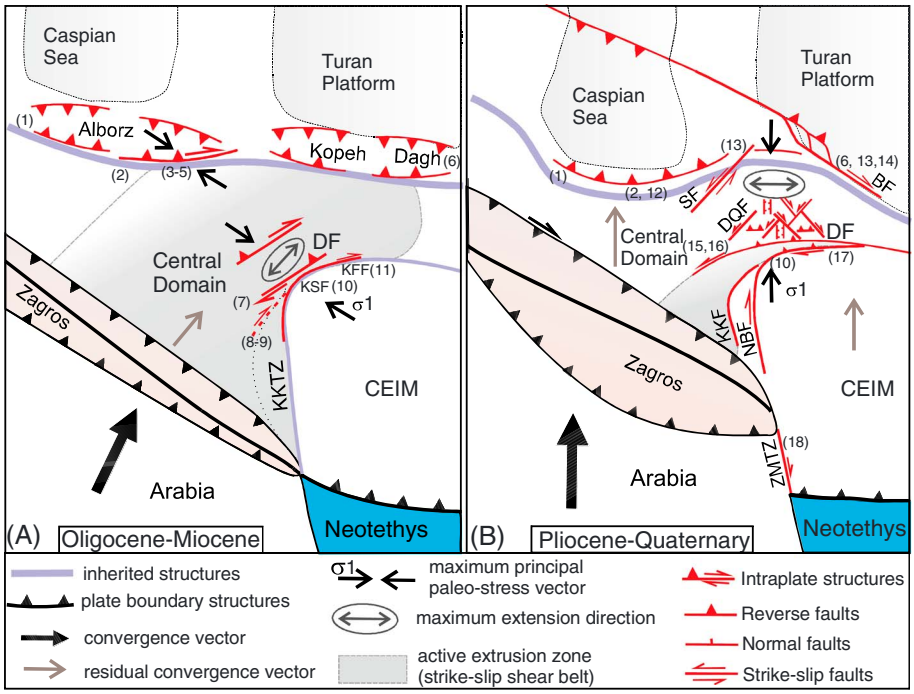

Figure 14. Conceptual spatiotemporal evolutionary model for the intraplate response to the Arabia-Eurasia convergence history as recorded in Central Iran during the last 25 Ma. (a) The early Miocene stage. (c) The Pliocene-Quaternary stage (modified and readapted after Allen et al., 2011; Ballato et al., 2011, 2013; Calzolari, Della Seta, et al., 2016; Calzolari, Rossetti, et al., 2016; Hollingsworth et al. (2010); Mattei et al., 2017; Mouthereau et al., 2012; Navabpour et al., 2007; Robert et al., 2014). Location of structures is only indicative. List of abbreviations: BF: Binalud fault; CEIM, Central East Iranian Microcontinent; DF: Doruneh fault; DQF: Dahan-Qaleh Fault; KFF: Kuh-e-Faghan fault; KKTZ: Kashmar-Kerman tectonic zone; KSF: Kuh-e-Sarhangi fault; NBF: Naiband fault; ZMTZ: Zagros-Makran transfer zone; SF: Shahroud fault. Numbers refer to the tectonostratigraphic and timing constraints available from the literature: (1) Madanipour et al. (2013, 2017), (2) Rezaeian et al. (2012); (3) Ballato et al. (2011); (4) Guest, Axen, et al. (2006); (5) Allen et al. (2003); (6) Robert et al. (2014); (7) Bagheri et al. (2016); (8) Karagaranbafghi et al. (2012); (9) Verdel et al. (2007); (10) Nozaem et al. (2013); (11) Calzolari, Della Seta, et al. (2016); (12) Cifelli et al. (2015); (13) Hollingsworth et al., (2010); (14) Shabanian et al. (2012); (15) Javadi et al. (2015); (16) Bagheri et al. (2016); (17) Calzolari, Rossetti, et al. (2016); (18) Regard et al. (2005; 2010).

and uplift along the Zagros collisional zone, and, in part, transferred northward through central Iran to the Alborz and Kopeh Dagh regions, where a major episode of positive tectonic inversion occurred (Agard et al., 2005; François et al., 2014; Madanipour et al., 2013, 2017; Mouthereau et al., 2012; Robert et al., 2014).

In the early to middle Miocene, the Arabia-Eurasia collision system entered into a mature stage with an increase in plate coupling, and the consequent intraplate stress transfer resulted in renewed intraplate shortening (Figure 14a). This new geodynamic configuration imposed a northeastward escape component to the intraplate domain of Central Iran due to the wedge-shaped geometry defined by the roughly E-W trending Alborz-Kopeh Dagh accommodation zone to the north and by the western-northwest boundary of the CEIM. To the north, dextral transpression has been documented in Central Alborz from early Miocene to late Miocene in response to a NW-SE directed shortening direction (Allen et al., 2003; Ballato et al., 2011; Guest, Axen, et al., 2006; Landgraf et al., 2009; Zanchi et al., 2006). In Central Iran, Miocene distributed dextral shearing is documented along the Kuh-Sarhangi Fault (Nozaem et al., 2013), Kuh-e-Faghan Fault (Calzolari, Della Seta, et al., 2016), and the DF region (Javadi et al., 2013; this study) (Figure 1). Coeval dextral shearing is also documented during the tectonic reactivation of the Kashmar Kerman Tectonic Zone (Karagaranbafghi et al., 2012; Verdel et al., 2007) (Figures 1 and 14a), where a prolonged history of deformation and magmatism is recorded since the late Proterozoic (Ramezani & Tucker, 2003; Rossetti et al., 2015). It thus emerges that at least during the early to late Miocene a major, crustal-scale dextral shear belt existed within the hinterland domain of the Zagros convergence zone, largely accommodated along the Alborz Range and southern regions along the boundary with the CEIM (along the Doruneh, Kuh-e-Sarhangi, and Kuh-e-Faghan fault systems; Figure 14a). In this view, the early NW-SE maximum compression direction documented across

the DF region and the Alborz Range is therefore here interpreted as a kinematic stress field generated at the NW boundary of the CEIM within a general scenario of NE directed extrusion of the intraplate domain during progress of the continental collision at the convergence front. The resulting far-field stress was largely accommodated through tectonic reactivation of the inherited Mesozoic rift structures in Central Iran that were lately by-passed during propagation of dextral shearing in the intracontinental domain (Figure 14a).

At the Miocene-Pliocene boundary, the deformation regime in Central Iran changed, in response to a switch to a NS oriented convergence direction along the Zagros collisional margin (Allen et al., 2004; McQuarrie et al., 2003; Navabpour et al., 2007) (Figure 14b). At that time, the Alborz and Kopeh Dagh deformation zones were not able to accommodate the compressional stresses transmitted from the Zagros collisional zone that was also probably too thick to sustain further shortening during ongoing convergence (e.g., Allen et al., 2011; Austermann & Iaffaldano, 2013). The rigid blocks of the Caspian Sea to the west and the Turan plate to the east then became then part of the intraplate deformation domain. This new stress regime was in part accommodated by dextral transpression along the Zagros-Makran Transfer Zone (Regard et al., 2005) and by a major kinematic change from range parallel dextral to sinistral strike-slip tectonics in Central Alborz (Allen et al., 2003; Ballato et al., 2011, 2013; Guest, Axen, et al., 2006). In Central Iran, far-field propagation of the residual stress generated at the collisional boundary resulted in the development of N-S striking dextral strike-slip fault systems bounding and dissecting the CEIM along the boundaries of the constituent tectonic blocks (Yazd, Tabas, and Lut; see also Konon et al., 2016). The northward motion of the CEIM was dominantly accommodated to the north by the oroclinal bending of the Alborz Range (Cifelli et al., 2015; Hollingsworth et al., 2010; Mattei et al., 2017), which occurred in conjunction with the activation of NW-SE dextral Binalud Fault in Kopeh Dagh (Shabanian et al., 2010) and by the NE-SW sinistral Shahrud Fault along the eastern Alborz Range (Hollingsworth et al., 2010) (Figure 1). We infer that after oroclinal bending stopped along the Aborz-Kopeh Dagh belt, the accommodation zone of the residual component of the NS convergence in intraplate Central Iran expanded southward to the Cenozoic deformation zone described in this study. The region to the south of the Alborz-Kopeh Dagh zone (the DF region) mechanically acted as a rigid block in response to the continuous NS directed shortening, being cut across by conjugate sets of NW-SE dextral and NE-SW sinistral faults strands as documented to the north of the active trace of the DF region (Berberian, 2014; Farbod et al., 2011; Hollingsworth et al., 2010; Javidfakhr et al., 2011; Khodaverdian et al., 2015; Shabanian et al., 2010) (Figure 14b). In this context, the Quaternary sinistral/reverse shearing along the active trace of the DF has been accompanied by concurrent dextral shearing along the E-W Kuh-e-Faghan Fault, about 20 km to the south (Calzolari, Della Seta, et al., 2016; Calzolari, Rossetti, et al., 2016; Nozaem et al., 2013) (Figures 1 and 2). As a consequence, we also infer a progressive spatiotemporal southward migration in escape/extrusion tectonics as controlled by the space-time evolution of the convergence accommodation zones in intraplate Central Iran (Figure 14b).

It is worth noting that the regional stress changes from NW-SE to N-S and then to NE-SW in the eastern Alborz and Kopeh Dagh mountains have occurred after the Miocene-Pliocene tectonic reorganization of the Iran region, likely since the early Quaternary (Shabanian, Siame, et al., 2009). In this context, the dominant sinistral shearing documented along the active trace of the DF and the present seismotectonic scenario of the DF region (Farbod et al., 2011; Fattahi et al., 2007; Zarifi et al., 2013) (Figure 2) can be also ascribed to the prevailing effects of the modern state of stress (NE directed σ_1) of NE Iran.

8. Conclusion

The integration of structural and low-temperature thermochronological data collected from this study documents that in post-Eocene times the region to the north of the active trace of the DF operated as a major shear belt in intraplate Central Iran.

Results document a polyphase tectonic evolution, where three main deformation and exhumation stages are recognized: (i) at the Eocene-Oligocene boundary, (ii) at the early Miocene (22–18 Ma), and (iii) a final episode of enhanced cooling/exhumation during the Miocene-Pliocene boundary (at approximately 5 Ma). The latter is here referred to a major shift in the maximum compression direction from a NW-SE to a N-S orientation, when the region was cut across by distributed NW-SE dextral and NE-SW sinistral conjugate fault systems.

The geological evidence presented in this study (i) proves the DF region registered a long-lived tectonic evolution during which it operated as a major dextral accommodation zone in intraplate Central Iran in

post-Eocene times and (ii) demonstrates the sinistral shearing recorded along the active trace of the DF represents the last shear increment (likely late Quaternary in age) at the northern boundary of the CEIM, in response to a major regional tectonic reorganization initiated at the Miocene-Pliocene boundary.

The pulsed tectonic evolution documented in this study well correlates with the main regional tectonic/geodynamic events recorded along the Bitlis-Zagros convergence zone, suggesting (i) the DF region operated as a major zone or residual stress transfer and accommodation in intraplate Central Iran in post-Eocene times and (ii) the tectonic evolution of the DF region was modulated by the convergent plate-boundary dynamics and the modes of tectonic reactivation of the inherited intracontinental weak zones located in its hinterland domains (Alborz, Kopeh Dagh, and Central Domain structural zones in Figure 1).

Appendix A

A1. Fault Population Analysis

Fault population analysis was carried out through the Daisy software v.5.22e. (Structural Data Integrated System Analyzer; free available at http://host.uniroma3.it/progetti/fralab/)

A1.1. Polymodal Gaussian Analysis

Statistical analyses of single parameters include fault strikes, fault dips, and slickenline pitches. These analyses were performed to identify the fault subsets and to associate data with them, as well as to describe their spatial variation through the studied region. The analysis is based on the comparison (best fit) of the frequency of the considered parameter with a family of circular Gaussian Curves that replicate the independent populations in a polymodal distribution. This methodology follows the approach in Wise et al. (1985), where it has successfully applied to lineament analysis of pseudo-radar images. The spatial distribution analyses refers to the methodology presented in Salvini et al. (1999). We refer to these articles for the complete explanation of the methodology. In the present work, the Gaussian best fit was performed in all analyses assuming a maximum of 10 Gaussian Curves (i.e., up to 10 independent data populations), and Sensitivity (90) and Resolution values (50) that correspond to concentrate the inversion for each single Gaussian curve within an interval equal to their width at half high, and a minimum peak high for the initial detection of 20% of the maximum frequency value in the frequency histogram. These initial values can change during the inversion process that is based on a cyclic convergence process.

A1.2. Multiple-Stress Statistic Inversion (Rotax Analysis)

The fault inversion of the fault slip data was analyzed by considering their generation according to the Coulomb Failure Criterion (Salvini & Vittori, 1982). The method assumes that all faults were generated with the most efficient orientation with respect to the acting stress tensor, which corresponds to the classical conjugate set of faults forming respectively an angle $\alpha = 45° - \phi/2$ to the σ_1 and an angle $\alpha' = 90° - \alpha$ to the σ_3 orientations, where ϕ is the internal friction angle. As a geometric consequence, the line on the fault plane normal to the slip vector lies parallel to the σ_2. This element is named rotational axis (Wise & Vincent, 1965), rotax (Salvini & Vittori, 1982), or slip normal; and faults generated by the same stress condition will have the rotaxes clustered around the σ_2 of the responsible stress. In the inversion process, faults are grouped according to the found clusters of rotaxes in the contouring on a stereographic projection. Each cluster corresponds to a possible orientation of the σ_2 of the paleostresses responsible for the faulting. In this iteration, the minimum angular distance from two adjacent rotax concentrations to be considered as separate subsets is set to 25°. Faults of each rotax cluster have slip vectors along the great circle normal to the cluster. Clustering of slip vectors along this circle and their relative sense of movements is analyzed to detect the σ_1/σ_3 of the stress tensor responsible for the fault failure of the corresponding fault subset (i.e., having similar orientations of σ_1/σ_3 and rotax/σ_2). In the case of strike-slip faulting, as in the studied region, since all the fault subsets share the same near-vertical rotax/σ_2 attitude, the possible independent subsets are discriminated by first by the strike and movement sense of the faults. The method then identifies the possible conjugate sets to recognize the paleostress event(s) responsible for the faulting. The accuracy of the stress inversion results are tested through the mean deviation angle (i.e., MAD, the mean angle of deviation between the predicted and calculated slip vectors); acceptable results are those for which this value is $<30°$ (Nur et al., 1986). Due to the fact that this method has a statistical approach, users have to select the least number of faults that can justify each proposed stress field as well as the confidence of the scattering of data in the cluster. Again,

the fraction of faults belonging to the proposed paleostress orientations provides the estimation of the robustness of the results.

A2. Apatite Thermochronology

The apatite grains were recovered from the collected samples following standard crushing, sieving, washing, magnetic, and heavy liquid separation.

A2.1. Apatite Fission Track thermochronology (AFT)

Apatite grains were mounted in Araldite® adhesive, ground, and polished to expose internal mineral surfaces. Etching with 5.5 M of HNO3 at room temperature for 20 s revealed spontaneous fission tracks intersecting the apatite surface. Samples were covered with a uranium free muscovite external detector and irradiated with thermal neutrons at the Radiation Center of the Oregon State University. Induced fission tracks in the external detector were revealed by etching the mounts in 40% HF at room temperature for 40 min. The fission tracks were counted by the first author under a nominal magnification of 1250X on an Olympus BX51 equipped with an automatic stage and a videocamera (at the Thermochronology Laboratory, Department of Geosciences, University of Padova). The single-grain age distribution of each sample was decomposed into age populations that fit the measured distribution by using the best fit binomial peak fitting method (Galbraith & Green, 1990). The Track key 4.2 Program was used for all AFT age calculations procedures (Dunkl, 2002). A chi-square (χ^2) test is carried out on the AFT single-grain age in order to test the homogeneity of data (Galbraith, 1981). The probability of (χ^2) is calculated for each sample; if $P(\chi^2) > 5\%$ then the sample is assumed to be homogenous (Galbraith & Laslett, 1993).

A2.2. Apatite Uranium-Thorium/Helium Thermochronology

The AHe analyses were carried out at Arizona University. Euhedral apatites were picked using a cross-polarized binocular microscope. Most grains had a minimum diameter of 90 μm and were inclusion free to avoid effects of He-implanting from inclusions or excess loss of He during decay due to a large surface/volume ratio (Farley, 2000). The grain dimensions were measured for calculation of the alpha-ejection (Ft) correction factor after Farley et al. (1996), and single grains were packed in Nb-tubes for U-Th/He measurement. For each sample three aliquots were prepared for analysis in order to ensure sample age reproducibility. The concentration of ^{4}He was determined by the ^{3}He isotope dilution and measurement of the ^{4}He/^{3}He ratio through a quadrupole mass spectrometer. Apatite samples were heated for 5 min at 11 Amps with a 960 nm diode laser for degassing. Each sample was reheated and measured to ensure that all gas was extracted in the first run. U, Th concentrations were obtained by isotope dilution using an inductively coupled plasma mass spectrometer. The HeFTY 1.9 program was used for AHe thermal modeling (Ketcham, 2005).

Acknowledgments

Special thanks go to M. R. Mazinani, A. Rabiee, P. Khodabakhshi, and F. Lucci for assistance during field work. C. Faccenna and A Yassaghi are thanked for advice and support. We would like to thank the manager and the staff of Khaneh-e-Moallem of Kashmar for their kind hospitality. We also thank Ali Rastpour, Hassan Faraji, and Mehdi Miri for driving to the field and logistic support. The first author would like also to thank Shabnam Jafari, Valentino Dall'Acqua, Sandra Boesso and Benedetta Andreucci are warmly thanked for their help during preparation of apatite samples at the University of Padova. We gratefully acknowledge the Kashmar Gubernatorial and its kind staff for all logistic support during our fieldwork. We also thank the Imam Khomeini International University, Qazvin, for continuous support. The manuscript benefitted of constructive comments and advice from E. Shabanian, an anonymous reviewer and the AE B. Guest. Data in support of this study can be found in the supporting information (SI) to the paper. This study is part of the research activity carried out during the first author's PhD research at the Roma Tre University.

References

Agard, P., Omrani, J., Jolivet, L., & Mouthereau, F. (2005). Convergence history across Zagros (Iran): Constraints from collisional and earlier deformation. *International Journal of Earth Sciences*, *94*(3), 401–419. https://doi.org/10.1007/s00531-005-0481-4

Agard, P., Omrani, J., Jolivet, L., Whitechurch, H., Vrielynck, B., Spakman, W., … Wortel, R. (2011). Zagros orogeny: A subduction-dominated process. *Geological Magazine*, *148*(5-6), 692–725. https://doi.org/10.1017/S001675681100046X

Allen, M. B., & Armstrong, H. A. (2008). Arabia-Eurasia collision and the forcing of mid-Cenozoic global cooling. *Palaeogeography, Palaeoclimatology, Palaeoecology*, *265*(1-2), 52–58. https://doi.org/10.1016/j.palaeo.2008.04.021

Allen, M., Ghassemi, M. R., Shahrabi, M., & Qorashi, M. (2003). Accommodation of late Cenozoic oblique shortening in the Alborz range, northern Iran. *Journal of Structural Geology*, *25*(5), 659–672. https://doi.org/10.1016/S0191-8141(02)00064-0

Allen, M., Jackson, J., & Walker, R. (2004). Late Cenozoic reorganization of the Arabia-Eurasia collision and the comparison of short-term and long-term deformation rates. *Tectonics*, *23*, TC2008. https://doi.org/10.1029/2003TC001530

Allen, M. B., Kheirkhah, M., Emami, M. H., & Jones, S. J. (2011). Right-lateral shear across Iran and kinematic change in the Arabia-Eurasia collision zone. *Geophysical Journal International*, *184*(2), 555–574. https://doi.org/10.1111/j.1365-246X.2010.04874.x

Ambraseys, N. N., & Melville, C. P. (1982). *A history of Persian earthquakes*. Cambridge, UK: Cambridge University press.

Austermann, J., & laffaldano, G. (2013). The role of the Zagros orogeny in slowing down Arabia-Eurasia convergence since~ 5 Ma. *Tectonics*, *32*, 351–363. https://doi.org/10.1002/tect.20027

Authemayou, C., Chardon, D., Bellier, O., Malekzadeh, Z., Shabanian, E., & Abbassi, M. R. (2006). Late Cenozoic partitioning of oblique plate convergence in the Zagros fold-and-thrust belt (Iran). *Tectonics*, *25*, TC3002. https://doi.org/10.1029/2005TC001860

Avouac, J. P., & Tapponnier, P. (1993). Kinematic model of active deformation in central Asia. *Geophysical Research Letters*, *20*(10), 895–898. https://doi.org/10.1029/93GL00128

Axen, G. J., Lam, P., Grove, S. M., Stockli, D. F., & Hassanzadeh, J. (2001). Exhumation of the west-central Alborz Mountains, Iran, Caspian subsidence, and collision-related tectonics. *Geology*, *29*(6), 559–562. https://doi.org/10.1130/0091-7613(2001)029%3C0559:EOTWCA%3E2.0.CO;2

Bagheri, S., Madhanifard, R., & Zahabi, F. (2016). Kinematics of the Great Kavir fault inferred from a structural analysis of the Pees Kuh Complex, Jandaq area, central Iran. *Geological Society of America Special Papers*, *525*(6). https://doi.org/10.1130/2016.2525

Ballato, P., Nowaczyk, N. R., Landgraf, A., Strecker, M. R., Friedrich, A., & Tabatabaei, S. H. (2008). Tectonic control on sedimentary facies pattern and sediment accumulation rates in the Miocene foreland basin of the southern Alborz mountains, northern Iran. *Tectonics*, *27*, TC6001. https://doi.org/10.1029/2008TC002278

Ballato, P., Stockli, D. F., Ghassemi, M. R., Landgraf, A., Strecker, M. R., Hassanzadeh, J., … Tabatabaei, S. H. (2013). Accommodation of transpressional strain in the Arabia-Eurasia collision zone: New constraints from (U-Th)/He thermochronology in the Alborz mountains, north Iran. *Tectonics*, *32*, 1–18. https://doi.org/10.1029/2012TC003159

Ballato, P., Uba, C. E., Landgraf, A., Strecker, M. R., Sudo, M., Stockli, D. F., … Tabatabaei, S. H. (2011). Arabia-Eurasia continental collision: Insights from late Tertiary foreland-basin evolution in the Alborz Mountains, Northern Iran. *Geological Society of America Bulletin*, *123*(1-2), 106–131. https://doi.org/10.1130/B30091.1

Barrier, E. & Vrielynck, B. (2008). Palaeotectonic map of the Middle East, Atlas of 14 maps, tectonosedimentary-palinspastic maps from Late Norian to Pliocene. Commission for the Geologic Map of the World (CCMW, CCGM), Paris.

Behroozi, A., Sahbaei, M., Etemadi, N., Zedeh, A. A., Ghomashi, A., & Moghtader, M. (1987). *Geological map of Feyz Abad, 1:100000 scale*. Tehran: Geological Survey of Iran.

Berberian, M. (1974). A brief geological description of north-central Iran. In J. S. Tchalenko, et al. (Eds.), *Materials for the study of the seismotectonics of Iran North-Central Iran: Geological Survey of Iran Report* (Vol. 29, pp. 127–138). Tehran: Geological Survey of Iran.

Berberian, M. (1983). The southern Caspian: A compressional depression floored by a trapped, modified oceanic crust. *Canadian Journal of Earth Sciences*, *20*(2), 163–183. https://doi.org/10.1139/e83-015

Berberian, M. (2014). *Earthquakes and coseismic surface faulting on the Iranian Plateau; A historical, social and physical approach, first* (p. 776). Oxford: Elsevier Science.

Berberian, M., & King, G. C. P. (1981). Towards a paleogeography and tectonic evolution of Iran. *Canadian Journal of Earth Sciences*, *18*(11), 1764–1766. https://doi.org/10.1139/e81-163

Berra, F., Zanchi, A., Angiolini, L., Vachard, D., Vezzoli, G., Zanchetta, S., … Kouhpeyma, M. (2017). The upper Palaeozoic Godar-e-Siah complex of Jandaq: Evidence and significance of a north Palaeotethyan succession in Central Iran. *Journal of Asian Earth Sciences*, *138*, 272–290. https://doi.org/10.1016/j.jseaes.2017.02.006

Burtner, R. L., Nigrini, A., & Donelick, R. A. (1994). Thermochronology of Lower Cretaceous source rocks in the Idaho-Wyoming thrust belt. *The American Association of Petroleum Geologists Bulletin*, *78*(10), 1613–1636. https://doi.org/10.1306/A25FF233-171B-11D7-8645000102C1865D

Calzolari, G., Della Seta, M., Rossetti, F., Nozaem, R., Vignaroli, G., Cosentino, D., & Faccenna, C. (2016). Geomorphic signal of active faulting at the northern edge of Lut Block: Insights on the kinematic scenario of Central Iran. *Tectonics*, *35*, 76–102. https://doi.org/10.1002/2015TC003869

Calzolari, G., Rossetti, F., Della Seta, M., Nozaem, R., Olivetti, V., Balestrieri, M. L., … Vignaroli, G. (2016). Spatio-temporal evolution of intraplate strike-slip faulting: The Neogene-Quaternary Kuh-e-Faghan Fault, central Iran. *Geological Society of America Bulletin*, *128*(3-4), 374–396. https://doi.org/10.1130/B31266.1

Cifelli, F., Ballato, P., Alimohammadian, H., Sabouri, J., & Mattei, M. (2015). Tectonic magnetic lineation and oroclinal bending of the Alborz range: Implications on the Iran-southern Caspian geodynamics. *Tectonics*, *34*, 116–132. https://doi.org/10.1002/2014TC003626

Cloetingh, S., Ziegler, P. A., Beekman, F. P., Andriessen, A. M., Matenco, L., Bada, G., … Sokoutis, D. (2005). Lithospheric memory, state of stress and rheology: Neotectonic controls on Europe's intraplate continental topography. *Quaternary Science Reviews*, *24*(3-4), 241–304. https://doi.org/10.1016/j.quascirev.2004.06.015

Cunningham, D., Dijkstra, A., Howard, J., Quarles, A., & Badarch, G. (2003). Active intraplate strike-slip faulting and transpressional uplift in the Mongolian Altai. *Geological Society of London, Special Publication*, *210*(1), 65–87. https://doi.org/10.1144/GSL.SP.2003.210.01.05

Davis, G. H., Bump, A. P., Garcia, P. E., & Ahlgren, S. G. (1999). Conjugate Riedel deformation band shear zones. *Journal of Structural Geology*, *22*(2), 169–190. https://doi.org/10.1016/S0191-8141(99)00140-6

Davoudzadeh, M., Soffel, H., & Schmidt, K. (1981). On the rotation of the Central-East Iran microplate. Neues Jahrbuch für Geologie und Paläontologie. *Monatshefte*, *1981*(3), 180–192.

Di Vincenzo, G., Rossetti, F., Viti, C., & Balsamo, F. (2013). Constraining the timing of fault reactivation: Eocene coseismic slip along a Late Ordovician ductile shear zone (northern Victoria Land, Antarctica). *Geological Society of America Bulletin*, *125*(3-4), 609–624. https://doi.org/10.1130/B30670.1

Djamour, Y., Vernant, P., Bayer, R., Nankali, H. R., Ritz, J. F., Hinderer, J., … Khorrami, F. (2010). GPS and gravity constraints on continental deformation in the Alborz mountain range, Iran. *Geophysical Journal International*, *183*(3), 1287–1301. https://doi.org/10.1111/j.1365-246X.2010.04811.x

Doblas, M. (1998). Slickenside kinematic indicators. *Tectonophysics*, *295*(1-2), 187–197. https://doi.org/10.1016/S0040-1951(98)00120-6

Dunkl, I. (2002). Trackkey: A windows program for calculation and graphical presentation of fission track data. *Computers & Geosciences*, *28*(1), 3–12. https://doi.org/10.1016/S0098-3004(01)00024-3

Eftekhar-Nezhad, J., Aghanabati, A., Hamzehpour, B., & Baroyant, V. (1976). *Geological map of Kashmar, scale 1:250,000*. Tehran: Geological Survey of Iran.

Ellis, S. (1996). Forces driving continental collision: Reconciling indentation and mantle subduction tectonics. *Geology*, *24*(8), 699–702. https://doi.org/10.1130/0091-7613(1996)024%3C0699:FDCCRI%3E2.3.CO;2

Farbod, Y., Bellier, O., Shabanian, E., & Abbassi, M. R. (2011). Geomorphic and structural variations along the Doruneh Fault System (central Iran). *Tectonics*, *30*, TC6014. https://doi.org/10.1029/2011TC002889

Farbod, Y., Shabanian, E., Bellier, O., Abbassi, M. R., Braucher, R., Benedetti, L., … Hessami, K. (2016). Spatial variations in late Quaternary slip rates along the Doruneh Fault System (Central Iran). *Tectonics*, *35*, 386–406. https://doi.org/10.1002/2015TC003862

Farley, K. A. (2000). Helium diffusion from apatite: General behavior as illustrated by Durango fluorapatite. *Journal of Geophysical Research*, *105*(B2), 2903–2914. https://doi.org/10.1029/1999JB900348

Farley, K. A., Wolf, R. A., & Silver, L. T. (1996). The effects of long alpha-stopping distances on (U- Th)/He ages. *Geochimica et Cosmochimica Acta*, *60*(21), 4223–4229. https://doi.org/10.1016/S0016-7037(96)00193-7

Fattahi, M., Walker, R. T., Khatib, M. M., Dolati, A., & Bahroudi, A. (2007). Slip-rate estimate and past earthquakes on the Doruneh fault, eastern Iran. *Geophysical Journal International*, *168*(2), 691–709. https://doi.org/10.1111/j.1365-246X.2006.03248.x

Foroutan, M., Meyer, B., Sébrier, M., Nazari, H., Murray, A. S., Le Dortz, K., … Keddadouche, K. (2014). Late Pleistocene-Holocene right slip rate and paleoseismology of the Nayband fault, western margin of the Lut block, Iran. *Journal of Geophysical Research: Solid Earth*, *119*, 3517–3560. https://doi.org/10.1002/2013JB010746

Foroutan, M., Sébrier, M., Nazari, H., Meyer, B., Fattahi, M., Rashidi, A., … Bateman, M. D. (2012). New evidence for large earthquakes on the Central Iran plateau: Palaeoseismology of the Anar fault. *Geophysical Journal International*, *189*(1), 6–18. https://doi.org/10.1111/j.1365-246X.2012.05365.x

Fossen, H. (2010). *Structural geology, first* (p. 480). Cambridge, UK: Cambridge University Press. https://doi.org/10.1017/CBO9780511777806
François, T., Agard, P., Bernet, M., Meyer, B., Chung, S. L., Zarrinkoub, M. H., … Monié, P. (2014). Cenozoic exhumation of the internal Zagros: First constraints from low-temperature thermochronology and implications for the build-up of the Iranian plateau. *Lithos*, *206-207*(1), 100–112. https://doi.org/10.1016/j.lithos.2014.07.021
Galbraith, R. F. (1981). On statistical models for fission track counts. *Mathematical Geology*, *13*(6), 471–478. https://doi.org/10.1007/BF01034498
Galbraith, R. F., & Green, P. F. (1990). Estimating the component ages in a finite mixture. *International Journal of Radiation Applications and Instrumentation. Part D. Nuclear Tracks and Radiation Measurements*, *17*(3), 197–206. https://doi.org/10.1016/1359-0189(90)90035-V
Galbraith, R. F., & Laslett, G. M. (1993). Statistical models for mixed fission track ages. *International Journal of Radiation Applications and Instrumentation. Part D. Nuclear Tracks and Radiation Measurements*, *21*(4), 459–470. https://doi.org/10.1016/1359-0189(93)90185-C
Gavillot, Y., Axen, G. J., Stockli, D. F., Horton, B. K., & Fakhari, M. D. (2010). Timing of thrust activity in the High Zagros fold-thrust belt, Iran, from (U-Th)/He thermochronometry. *Tectonics*, *29*, TC4025. https://doi.org/10.1029/2009TC002484
Ghaemi, F., & Moussavi Herami, R. (2008). *Geological map of Doruneh, 1:100000 scale*. Tehran: Geological Survey of Iran.
Ghods, A., Shabanian, E., Bergman, E., Faridi, M., Donner, S., Mortezanejad, G., & Aziz-Zanjani, A. (2015). The Varzaghan–Ahar, Iran, Earthquake Doublet (M_w 6.4, 6.2): Implications for the geodynamics of northwest Iran. *Geophysical Journal International*, *203*(1), 522–540. https://doi.org/10.1093/gji/ggv306
Green, P. F., & Duddy, I. R. (1989). Some comments on paleotemperature estimation from apatite fission track analysis. *Journal of Petroleum Geology*, *12*(1), 111–114. https://doi.org/10.1306/BF9AB6A8-0EB6-11D7-8643000102C1865D
Guest, B., Axen, G. J., Lam, P. S., & Hassanzadeh, J. (2006). Late Cenozoic shortening in the west-central Alborz Mountains, northern Iran, by combined conjugate strike-slip and thin-skinned deformation. *Geosphere*, *2*(1), 35–52. https://doi.org/10.1130/GES00019.1
Guest, B., Horton, B. K., Axen, G. J., Hassanzadeh, J., & McIntosh, W. C. (2007). Middle to late Cenozoic basin evolution in the western Alborz Mountains: Implications for the onset of collisional deformation in northern Iran. *Tectonics*, *26*, TC6011. https://doi.org/10.1029/2006TC002091
Guest, B., Stockli, D. F., Grove, M., Axen, G. J., Lam, P. S., & Hassanzadeh, J. (2006). Thermal histories from the central Alborz Mountains, northern Iran: Implications for the spatial and temporal distribution of deformation in northern Iran. *Geological Society of America Bulletin*, *118*(11-12), 1507–1521. https://doi.org/10.1130/B25819.1
Hafkenscheid, E., Wortel, M. J. R., & Spakman, W. (2006). Subduction history of the Tethyan region derived from seismic tomography and tectonic reconstructions. *Journal of Geophysical Research*, *111*, B08401. https://doi.org/10.1029/2005JB003791
Hatzfeld, D., Authemayou, C., van der Beek, P., Bellier, O., Lave, J., Oveisi, B., … Yamini-Fard, F. (2010). The kinematics of the Zagros Mountains (Iran). *Geological Society, London, Special Publications*, *330*(1), 19–42. https://doi.org/10.1144/SP330.3
Hatzfeld, D., & Molnar, P. (2010). Comparisons of the kinematics and deep structures of the Zagros and Himalaya and of the Iranian and Tibetan plateaus and geodynamic implications. *Reviews of Geophysics*, *48*, RG2005. https://doi.org/10.1029/2009RG000304
Hessami, K., Koyi, H. A., Talbot, C. J., Tabasi, H., & Shabanian, E. (2001). Progressive unconformities within an evolving foreland fold-thrust belt, Zagros Mountains. *Journal of the Geological Society*, *158*(6), 969–981. https://doi.org/10.1144/0016-764901-007
Holdsworth, R., Strachan, R., & Dewey, J. (1998). Continental transpressional and transtensional tectonics. *Geological Society, London, Special Publications*, *135*, 307.
Hollingsworth, J., Fattahi, M., Walker, R., Talebian, M., Bahroudi, A., Bolourchi, M. J., … Copley, A. (2010). Oroclinal bending, distributed thrust and strike-slip faulting, and the accommodation of Arabia-Eurasia convergence in NE Iran since the Oligocene. *Geophysical Journal International*, *181*(3), 1214–1246. https://doi.org/10.1111/j.1365-246X.2010.04591.x
Homke, S., Vergés, J., Serra-Kiel, J., Bernaola, G., Sharp, I., Garcés, M., … Goodarzi, M. H. (2009). Late Cretaceous-Paleocene formation of the proto-Zagros foreland basin, Lurestan Province, SW Iran. *Geological Society of America Bulletin*, *121*(7-8), 963–978. https://doi.org/10.1130/B26035.1
Homke, S., Verges, J., van der Beek, P., Fernandez, M., Saura, E., Barbero, L., … Labrin, E. (2010). Insights in the exhumation history of the NW Zagros from bedrock and detrital apatite fission-track analysis: Evidence for a long-lived orogeny. *Basin Research*, *22*(5), 659–680. https://doi.org/10.1111/j.1365-2117.2009.00431.x
Jackson, J., & McKenzie, D. (1984). Active tectonics of the Alpine–Himalayan Belt between western Turkey and Pakistan. *Geophysical Journal International*, *77*(1), 185–264. https://doi.org/10.1111/j.1365-246X.1984.tb01931.x
Jafarian, M., Jalali, M., Mohammadi, O., & Nozari, A. (2000). *Geological map of Sheshtamad, 1:100000 scale*. Tehran: Geological Survey of Iran.
Javadi, H. R., Esterabi Ashtiani, M., Guest, B., Yassaghi, A., Ghassemi, M. R., Shahpasandzadeh, M., & Naeimi, A. (2015). Tectonic reversal of the western Doruneh Fault System: Implications for Central Asian tectonics. *Tectonics*, *34*, 2034–2051. https://doi.org/10.1002/2015TC003931
Javadi, H. R., Ghassemi, M. R., Shahpasandzadeh, M., Guest, B., Ashtiani, M. E., Yassaghi, A., & Kouhpeyma, M. (2013). History of faulting on the Doruneh Fault System: Implications for the kinematic changes of the Central Iranian Microplate. *Geological Magazine*, *150*(04), 651–672. https://doi.org/10.1017/S0016756812000751
Javidfakhr, B., Bellier, O., Shabanian, E., Ahmadian, S., & Saidi, A. (2011). Plio-Quaternary tectonic regime changes in the transition zone between Alborz and Kopeh Dagh mountain ranges (NE Iran). *Tectonophysics*, *506*(1-4), 86–108. https://doi.org/10.1016/j.tecto.2011.04.013
Karagaranbafghi, F., Foeken, J. P. T., Guest, B., & Stuart, F. M. (2012). Cooling history of the Chapedony metamorphic core complex, Central Iran: Implications for the Eurasia-Arabia collision. *Tectonophysics*, *524-525*, 100–107. https://doi.org/10.1016/j.tecto.2011.12.022
Ketcham, R. a. (2005). Forward and inverse modeling of low-temperature thermochronometry data. *Reviews in Mineralogy and Geochemistry*, *58*(1), 275–314. https://doi.org/10.2138/rmg.2005.58.11
Ketcham, R. A., Carter, A., Donelick, R. A., Barbarand, J., & Hurford, A. J. (2007). Improved modeling of fission-track annealing in apatite. *American Mineralogist*, *92*(5-6), 799–810. https://doi.org/10.2138/am.2007.2281
Ketcham, R. A., Donelick, R. A., & Carlson, W. D. (1999). Variability of apatite fission-track annealing kinetics: III. Extrapolation to geological time scales. *American Mineralogist*, *84*(9), 1235–1255. https://doi.org/10.2138/am-1999-0903
Khadivi, S., Mouthereau, F., Barbarand, J., Adatte, T., & Lacombe, O. (2012). Constraints on palaeodrainage evolution induced by uplift and exhumation on the southern flank of the Zagros-Iranian Plateau. *Journal of the Geological Society*, *169*(1), 83–97. https://doi.org/10.1144/0016-76492011-031
Khadivi, S., Mouthereau, F., Larrasoana, J. C., Verges, J., Lacombe, O., Khademi, E., … Suc, J. P. (2010). Magnetochronology of synorogenic Miocene foreland sediments in the Fars arc of the Zagros Folded Belt (SW Iran). *Basin Research*, *22*(6), 918–932. https://doi.org/10.1111/j.1365-2117.2009.00446.x
Khodaverdian, A., Zafarani, H., & Rahimian, M. (2015). Long term fault slip rates, distributed deformation rates and forecast of seismicity in the Iranian Plateau. *Tectonics*, *34*, 2190–2220. https://doi.org/10.1002/2014TC003796
Konon, A., Nadimi, A., Koprianiuk, M., Wysocka, A., Szaniawski, R., Wyglądała, M., … Barski, M. (2016). Formation of intracontinental basins in the opposite corners of the Tabas block as coeval structures controlled by transpressional faulting, Iran. *Geological Society of America Bulletin*, *128*(11-12), 1593–1617. https://doi.org/10.1130/B31362.1

Landgraf, A., Ballato, P., Strecker, M. R., Friedrich, A., Tabatabaei, S. H., & Shahpasandzadeh, M. (2009). Fault-kinematic and geomorphic observations along the North Tehran Thrust and Mosha Fasham Fault, Alborz mountains Iran: Implications for fault-system evolution and interaction in a changing tectonic regime. *Geophysical Journal International*, *177*(2), 676–690. https://doi.org/10.1111/j.1365-246X.2009.04089.x

Le Dortz, K., Meyer, B., Sébrier, M., Braucher, R., Nazari, H., Benedetti, L., … Rashidi, A. (2011). Dating inset terraces and offset fans along the Dehshir Fault (Iran) combining cosmogenic and OSL methods. *Geophysical Journal International*, *185*(3), 1147–1174. https://doi.org/10.1111/j.1365-246X.2011.05010.x

Le Dortz, K., Meyer, B., Sébrier, M., Nazari, H., Braucher, R., Fattahi, M., … Talebian, M. (2009). Holocene right-slip rate determined by cosmogenic and OSL dating on the Anar fault, Central Iran. *Geophysical Journal International*, *179*(2), 700–710. https://doi.org/10.1111/j.1365-246X.2009.04309.x

Lesti, C., Giordano, G., Salvini, F., & Cas, R. (2008). Volcano tectonic setting of the intraplate, Pliocene-Holocene, Newer Volcanic Province (southeast Australia): Role of crustal fracture zones. *Journal of Geophysical Ressearch*, *113*, B07407. https://doi.org/10.1029/2007JB005110

Madanipour, S., Ehlers, T. A., Yassaghi, A., & Enkelmann, E. (2017). Accelerated middle Miocene exhumation of the Talesh Mountains constrained by U-Th/He thermochronometry: Evidence for the Arabia-Eurasia collision in the NW Iranian plateau. *Tectonics*, *36*, 1538–1561. https://doi.org/10.1002/2016TC004291

Madanipour, S., Ehlers, T. A., Yassaghi, A., Rezaeian, M., Enkelmann, E., & Bahroudi, A. (2013). Synchronous deformation on orogenic plateau margins: Insights from the Arabia-Eurasia collision. *Tectonophysics*, *608*, 440–451. https://doi.org/10.1016/j.tecto.2013.09.003

Mandl, G. (2000). *Faulting in brittle rocks. An introduction to the mechanics of tectonic faults* (p. 434). Berlin: Springer. https://doi.org/10.1007/978-3-662-04262-5

Masson, F., Anvari, M., Djamour, Y., Walpersdorf, A., Tavakoli, F., Daignières, M., … Van Gorp, S. (2007). Large-scale velocity field and strain tensor in Iran inferred from GPS measurements: New insight for the present-day deformation pattern within NE Iran. *Geophysical Journal International*, *170*(1), 436–440. https://doi.org/10.1111/j.1365-246X.2007.03477.x

Mattei, M., Cifelli, F., Alimohammadian, H., Rashid, H., Winkler, A., & Sagnotti, L. (2017). Oroclinal bending in the Alborz mountains (northern Iran): New constraints on the age of South Caspian subduction and extrusion tectonics. *Gondwana Research*, *42*, 13–28. https://doi.org/10.1016/j.gr.2016.10.003

Mattei, M., Cifelli, F., Muttoni, G., Zanchi, A., Berra, F., Mossavvari, F., & Eshraghi, S. A. (2012). Neogene block rotation in central Iran: Evidence from paleomagnetic data. *Geological Society of America Bulletin*, *124*(5-6), 943–956. https://doi.org/10.1130/B30479.1

McClusky, S., Reilinger, R., Mahmoud, M., Ben Sari, D., & Tealeb, A. (2003). GPS constraints on Africa and Arabia plate motions. *Geophysical Journal International*, *155*(1), 126–138. https://doi.org/10.1046/j.1365-246X.2003.02023.x

McQuarrie, N., Stock, J., Verdel, C., & Wernicke, B. (2003). Cenozoic evolution of Neotethys and implications for the causes of plate motions. *Geophysical Research Letters*, *30*(20), 2036. https://doi.org/10.1029/2003GL017992

Meyer, B., & Le Dortz, K. (2007). Strike-slip kinematics in central and eastern Iran: Estimating fault slip-rates averaged over the Holocene. *Tectonics*, *26*, TC5009. https://doi.org/10.1029/2006TC002073

Molnar, P. (1988). Continental tectonics in the aftermath of plate tectonics. *Nature*, *335*(6186), 131–137. https://doi.org/10.1038/335131a0

Molnar, P., & Lyon-Caen, H. (1988). Some simple physical aspects of the support, structure, and evolution of mountain belts. *Geological Society of America, Special Paper*, *218*, 179–208. https://doi.org/10.1130/SPE218-p179

Molnar, P., & Tapponnier, P. (1975). Cenozoic tectonics of Asia: Effects of a continental collision. *Science*, *189*(4201), 419–426. https://doi.org/10.1126/science.189.4201.419

Morley, C. K., Kongwung, B., Julapour, A. A., Abdolghafourian, M., Hajian, M., Waples, D., … Kazemi, H. (2009). Structural development of a major late Cenozoic basin and transpressional belt in central Iran: The Central Basin in the Qom-Saveh area. *Geosphere*, *5*(4), 325–362. https://doi.org/10.1130/GES00223.1

Mousavi, Z., Pathier, E., Walker, R. T., Walpersdorf, A., Tavakoli, F., Nankali, H., … Doin, M. P. (2015). Interseismic deformation of the Shahroud fault system (NE Iran) from space-borne radar interferometry measurements. *Geophysical Research Letters*, *42*, 5753–5761. https://doi.org/10.1002/2015GL064440

Mousavi, Z., Walpersdorf, A., Walker, R. T., Tavakoli, F., Pathier, E., Nankali, H., … Djamour, Y. (2013). Global Positioning System constraints on the active tectonics of NE Iran and the South Caspian region. *Earth and Planetary Science Letters*, *377-378*, 287–298. https://doi.org/10.1016/j.epsl.2013.07.007

Mouthereau, F., Lacombe, O., & Verges, J. (2012). Building the Zagros collisional orogen: Timing, strain distribution and the dynamics of Arabia/Eurasia plate convergence. *Tectonophysics*, *532-535*, 27–60. https://doi.org/10.1016/j.tecto.2012.01.022

Mouthereau, F., Tensi, J., Bellahsen, N., Lacombe, O., De Boisgrollier, T., & Kargar, S. (2007). Tertiary sequence of deformation in a thin-skinned/thick-skinned collision belt: The Zagros Folded Belt (Fars, Iran). *Tectonics*, *26*, TC5006. https://doi.org/10.1029/2007TC002098

Navabpour, P., Angelier, J., & Barrier, E. (2007). Cenozoic post-collisional brittle tectonic history and stress reorientation in the High Zagros Belt (Iran, Fars Province). *Tectonophysics*, *432*(1-4), 101–131. https://doi.org/10.1016/j.tecto.2006.12.007

Nazari, H., Fattahi, M., Meyer, B., Sébrier, M., Talebian, M., Foroutan, M., … Ghorashi, M. (2009). First evidence for large earthquakes on the Deshir Fault, Central Iran Plateau. *Terra Nova*, *21*(6), 417–426. https://doi.org/10.1111/j.1365-3121.2009.00892.x

Niu, Y., O'Hara, M. J., & Pearce, J. A. (2003). Initiation of subduction zones as a consequence of lateral compositional buoyancy contrast within the lithosphere: A petrological perspective. *Journal of Petrology*, *44*(5), 851–866. https://doi.org/10.1093/petrology/44.5.851

Nozaem, R., Mohajjel, M., Rossetti, F., Della Seta, M., Vignaroli, G., Yassaghi, A., … Eliassi, M. (2013). Post-Neogene right-lateral strike–slip tectonics at the north-western edge of the Lut Block (Kuh-e-Sarhangi Fault), Central Iran. *Tectonophysics*, *589*, 220–233. https://doi.org/10.1016/j.tecto.2013.01.001

Nur, A., Ron, H., & Scotti, O. (1986). Fault mechanics and the kinematics of block rotations. *Geology*, *14*(9), 746–749. https://doi.org/10.1130/0091-7613(1986)14%3C746:FMATKO%3E2.0.CO;2

Okay, A. I., Zattin, M., & Cavazza, W. (2010). Apatite fission-track data for the Miocene Arabia-Eurasia collision. *Geology*, *38*(1), 35–38. https://doi.org/10.1130/G30234.1

Petit, J. P. (1987). Criteria for the sense of movement on fault surfaces in brittle rocks. *Journal of Structural Geology*, *9*(5-6), 597–608. https://doi.org/10.1016/0191-8141(87)90145-3

Pezzo, G., Tolomei, C., Atzori, S., Salvi, S., Shabanian, E., Bellier, O., & Farbod, Y. (2012). New kinematic constraints of the western Doruneh fault, northeastern Iran, from interseismic deformation analysis. *Geophysical Journal International*, *190*(1), 622–628. https://doi.org/10.1111/j.1365-246X.2012.05509.x

Ramezani, J., & Tucker, R. D. (2003). The Saghand region, Central Iran: U-Pb geochronology, petrogenesis and implication for Gondwana tectonics. *American Journal of Science*, *303*(7), 622–665. https://doi.org/10.2475/ajs.303.7.622

Reece, R. S., Gulick, S. P. S., Christeson, G. L., Horton, B. K., Van Avendonk, H., & Barth, G. (2013). The role of farfield tectonic stress in oceanic intraplate deformation, Gulf of Alaska. *Journal of Geophysical Research: Solid Earth*, *118*, 1862–1872. https://doi.org/10.1002/jgrb.50177

Regard, V., Bellier, O., Thomas, J. C., Bourles, D., Bonnet, S., Abbassi, M. R., … Feghhi, K. (2005). Cumulative right-lateral fault slip rate across the Zagros-Makran transfer zone: Role of the Minab-Zendan fault system in accommodating Arabia-Eurasia convergence in southeast Iran. *Geophysical Journal International*, *162*(1), 177–203. https://doi.org/10.1111/j.1365-246X.2005.02558.x

Regard, V., Hatzfeld, D., Molinaro, M., Aubourg, C., Bayer, R., Bellier, O., … Abbassi, M. (2010). The transition between Makran subduction and the Zagros collision: Recent advances in its structure and active deformation. *Geological Society, London, Special Publications*, *330*(1), 43–64. https://doi.org/10.1144/SP330.4

Reilinger, R., McClusky, S., Vernant, P., Lawrence, S., Ergintav, S., Cakmak, R., … Nadariya, M. (2006). GPS constraints on continental deformation in the Africa-Arabia-Eurasia continental collision zone and implications for the dynamics of plate interactions. *Journal of Geophysical Research*, *111*, B05411. https://doi.org/10.1029/2005JB004051

Reuter, M., Piller, W. E., Harzhauser, M., Mandic, O., Berning, B., Rögl, F., … Hamedani, A. (2009). The Oligo-/Miocene Qom Formation (Iran): Evidence for an early Burdigalian restriction of the Tethyan Seaway and closure of its Iranian gateways. *International Journal of Earth Sciences*, *98*(3), 627–650. https://doi.org/10.1007/s00531-007-0269-9

Rezaeian, M., Carter, A., Hovius, N., & Allen, M. B. (2012). Cenozoic exhumation history of the Alborz Mountains, Iran: New constraints from low-temperature chronometry. *Tectonics*, *31*, TC2004. https://doi.org/10.1029/2011TC002974

Ritz, J. F., Nazari, H., Ghassemi, A., Salamati, R., Shafei, A., Solaymani, S., & Vernant, P. (2006). Active transtension inside central Alborz: A new insight into northern Iran-southern Caspian geodynamics. *Geology*, *34*(6), 477–480. https://doi.org/10.1130/G22319.1

Rizza, M., Shannon, A., Mahan, J. F. R., Nazari, H., Hollingsworth, J., & Salamati, R. (2011). Using luminescence dating of coarse matrix material to estimate the slip rate of the Astaneh fault, Iran. *Quaternary Geochronology*, *6*(3-4), 390–406. https://doi.org/10.1016/j.quageo.2011.03.001

Robert, A. M. M., Letouzey, J., Kavoosi, M. A., Sherkati, S., Müller, C., Vergés, J., & Aghababaei, A. (2014). Structural evolution of the Kopeh Dagh fold-and-thrust belt (NE Iran) and interactions with the South Caspian Sea Basin and Amu Darya Basin. *Marine and Petroleum Geology*, *57*, 68–87. https://doi.org/10.1016/j.marpetgeo.2014.05.002

Robertson, A. H. F., Ustaömer, T., Parlak, O., Ünlügenç, U. C., Taşli, K., & Inan, N. (2006). The Berit transect of the Tauride thrust belt, S Turkey: Late Cretaceous-Early Cenozoic accretionary/collisional processes related to closure of the Southern Neotethys. *Journal of Asian Earth Sciences*, *27*(1), 108–145. https://doi.org/10.1016/j.jseaes.2005.02.004

Rossetti, F., Nozaem, R., Lucci, F., Vignaroli, G., Gerdes, A., Nasrabadi, M., & Theye, T. (2015). Tectonic setting and geochronology of the Cadomian (Ediacaran-Cambrian) magmatism in Central Iran, Kuh-e-Sarhangi region (NW Lut Block). *Journal of Asian Earth Sciences*, *102*, 24–44. https://doi.org/10.1016/j.jseaes.2014.07.034

Salvini, F., Billi, A., & Wise, D. U. (1999). Strike-slip fault-propagation cleavage in carbonate rocks: The Mattinata Fault zone, southern Apennines, Italy. *Journal of Structural Geology*, *21*(12), 1731–1749. https://doi.org/10.1016/S0191-8141(99)00120-0

Salvini, F., & Vittori, E. (1982). Analisi strutturale della Linea Olevano-Antrodoco-Posta (Ancona-Anzio Auct.): Metodologia di studio delle deformazinoi fragili e presentazione del tratto meridionale. *Memorie della Società Geoligica Italiana*, *24*, 337–355.

Sella, G. F., Dixon, T. H., & Mao, A. (2002). REVEL: A model for recent plate velocities from space geodesy. *Journal of Geophysical Research*, *107*(B4), 2081. https://doi.org/10.1029/2000JB000033

Shabanian, E., Acocella, V., Gioncada, A., Ghasemi, H., & Bellier, O. (2012). Structural control on volcanism in intraplate post collisional settings: Late Cenozoic to Quaternary examples of Iran and Eastern Turkey. *Tectonics*, *31*, TC3013. https://doi.org/10.1029/2011TC003042

Shabanian, E., Bellier, O., Abbassi, M. R., Siame, L., & Farbod, Y. (2010). Plio-Quaternary stress states in NE Iran: Kopeh Dagh and Allah Dagh-Binalud mountain ranges. *Tectonophysics*, *480*(1-4), 280–304. https://doi.org/10.1016/j.tecto.2009.10.022

Shabanian, E., Bellier, O., Siame, L., Arnaud, N., Abbassi, M. R., & Cochemé, J. J. (2009). New tectonic configuration in NE Iran: Active strike-slip faulting between the Kopeh Dagh and Binalud mountains. *Tectonics*, *28*, TC5002. https://doi.org/10.1029/2008TC002444

Shabanian, E., Siame, L., Bellier, O., Benedetti, L., & Abbassi, M. R. (2009). Quaternary slip-rates along the north-eastern boundary of the Arabia-Eurasia collision zone (Kopeh Dagh Mountains, north-east Iran). *Geophysical Journal International*, *178*(2), 1055–1077. https://doi.org/10.1111/j.1365-246X.2009.04183.x

Shafaii Moghadam, H., Li, X. H., Ling, X. X., Santos, J. F., Stern, R. J., Li, Q. L., & Ghorbani, G. (2015). Eocene Kashmar granitoids (NE Iran): Petrogenetic constraints from U-Pb zircon geochronology and isotope geochemistry. *Lithos*, *216-217*(C), 118–135. https://doi.org/10.1016/j.lithos.2014.12.012

Shahrabi, M., Hosseini, K., Shabani, K., & Massomi, R. (2005). *Geological map of Bardaskan, 1:100000 scale*. Tehran: Geological Survey of Iran.

Simons, W. J. F., Socquet, A., Vigny, C., Ambrosius, B. A. C., Haji Abu, S., Promthong, C., … Spakman, W. (2007). A decade of GPS in Southeast Asia: Resolving Sundaland motion and boundaries. *Journal of Geophysical Research*, *112*, B06420. https://doi.org/10.1029/2005JB003868

Soffel, H. C., Schmidt, S., Davoudzadeh, M., & Rolf, C. (1996). New palaeomagnetic data from Central Iran and a Triassic palaeoreconstruction. *Geologische Rundschau*, *85*(2), 293–302. https://doi.org/10.1007/BF02422235

Soltani, A. (2000). Geochemistry and geochronology of I-type granitoid rocks in the northeastern central Iran plate, (doctoral dissertation). University of Wollongong, 320 p.

Stöcklin, J., & Nabavi, M. H. (1973). *Tectonic map of Iran, scale 1:250000*. Tehran: Geological Survey of Iran.

Storti, F., Holdsworth, R. E., & Salvini, F. (2003). Intraplate strike-slip deformation belts. *Geological Society of London, Special Publication*, *210*(1), 1–14. https://doi.org/10.1144/GSL.SP.2003.210.01.01

Storti, F., Rossetti, F., Läufer, A. L., & Salvini, F. (2006). Consistent kinematic architecture in the damage zones of intraplate strike-slip fault systems in North Victoria Land, Antarctica and implications for fault zone evolution. *Journal of Structural Geology*, *28*(1), 50–63. https://doi.org/10.1016/j.jsg.2005.09.004

Storti, F., Salvini, F., Rossetti, F., & Phipps Morgan, J. (2007). Intraplate termination of transform faulting within the Antarctic continent. *Earth and Planetary Science Letters*, *260*(1-2), 115–126. https://doi.org/10.1016/j.epsl.2007.05.020

Sylvester, A. G. (1988). Strike-slip faults. *Geological Society of America Bulletin*, *100*(11), 1666–1703. https://doi.org/10.1130/0016-7606(1988)100%3C1666:SSF%3E2.3.CO;2

Taheri, J., Shamanian, G., Shojai Kaveh, N., Rezai, M., Bahremend, M., Amirrazavi, M., … Hosseini, S. Z. (1998). *Geological map of Kashmar, 1:100000 scale*. Tehran: Geological Survey of Iran.

Talebian, M., & Jackson, J. (2004). A reappraisal of earthquake focal mechanisms and active shortening in the Zagros mountains of Iran. *Geophysical Journal International*, *156*(3), 506–526. https://doi.org/10.1111/j.1365-246X.2004.02092.x

Tavani, S., Mencos, J., Bausà, J., & Muñoz, J. A. (2011). The fracture pattern of the Sant Corneli Bóixols oblique inversion anticline (Spanish Pyrenees). *Journal of Structural Geology*, *33*(11), 1662–1680. https://doi.org/10.1016/j.jsg.2011.08.007

Tchalenko, J. S. (1968). The evolution of kink-bands and the development of compression textures in sheared clays. *Tectonophysics*, *6*(2), 159–174. https://doi.org/10.1016/0040-1951(68)90017-6

Tchalenko, J. S. (1973). The Kashmsr (Turshiz) 1903 and Torbat-e Heidariyeh (south) 1923 earthquakes in central Khorassan (Iran). *Annals of Geophysics*, *26*(1), 29–40.
Tchalenko, J., Berberian, M., & Behzadi, H. (1973). Geomorphic and seismic evidence for recent activity on the Doruneh Fault, Iran. *Tectonophysics*, *19*(4), 333–341. https://doi.org/10.1016/0040-1951(73)90027-9
Vahdati Daneshmand, F., & Nadim, H. (1999). *Geological map of Darin, 1:100000 scale*. Tehran: Geological Survey of Iran.
Van Hinsbergen, D. J. J., Cunningham, D., Straathof, G. B., Ganerød, M., Hendriks, B. W. H., & Dijkstra, A. H. (2015). Triassic to Cenozoic multi-stage intra-plate deformation focused near the Bogd Fault system, Gobi Altai, Mongolia. *Geoscience Frontiers*, *6*(5), 723–740. https://doi.org/10.1016/j.gsf.2014.12.002
Verdel, C., Wernicke, B. P., Ramezani, J., Hassanzadeh, J., Renne, P. R., & Spell, T. L. (2007). Geology and thermochronology of Tertiary Cordilleran-style metamorphic core complexes in the Saghand region of central Iran. *Geological Society of America Bulletin*, *119*(7-8), 961–977. https://doi.org/10.1130/B26102.1
Vernant, P., Nilforoushan, F., Hatzfeld, D., Abbassi, M. R., Vigny, C., Masson, F., … Chéry, J. (2004). Present-day crustal deformation and plate kinematics in the Middle East constrained by GPS measurements in Iran and northern Oman. *Geophysical Journal International*, *157*(1), 381–398. https://doi.org/10.1111/j.1365-246X.2004.02222.x
Vincent, S. J., & Allen, M. B. (2001). Sedimentary record of Mesozoic intracontinental deformation in the eastern Junggar Basin, northwest China: Response to orogeny at the Asian margin. *Memoir - Geological Society of America*, *194*, 341–360. https://doi.org/10.1130/0-8137-1194-0.341
Vincent, S. J., Morton, A. C., Carter, A., Gibbs, S., & Barabadze, T. G. (2007). Oligocene uplift of the western greater Caucasus: An effect of initial Arabia-Eurasia collision. *Terra Nova*, *19*(2), 160–166. https://doi.org/10.1111/j.1365-3121.2007.00731.x
Walker, R., & Jackson, J. (2004). Active tectonics and late Cenozoic strain distribution in central and eastern Iran. *American Geophysical Union: Tectonics*, *23*, 1–24. https://doi.org/10.1029/2003TC001529
Walpersdorf, A., Manighetti, I., Mousavi, Z., Tavakoli, F., Vergnolle, M., Jadidi, A., … Sedighi, M. (2014). Present-day kinematics and fault slip rates in eastern Iran, derived from 11 years of GPS data. *Journal of Geophysical Research. Solid Earth*, *119*, 1359–1383. https://doi.org/10.1002/2013JB010620
Wellman, H. W. (1966). Active wrench faults of Iran, Afghanistan and Pakistan. *Geologische Rundschau*, *55*(3), 716–735. https://doi.org/10.1007/BF02029650
Wise, D. U., Funiciello, R., Parotto, M., & Salvini, F. (1985). Topographic lineament swarms: Clues to their origin from domain analysis of Italy. *Geological Society of America Bulletin*, *96*(7), 952–967. https://doi.org/10.1130/0016-7606(1985)96%3C952:TLSCTT%3E2.0.CO;2
Wise, D. U., & Vincent, R. J. (1965). Rotation axis method for detecting conjugate planes in calcite petrofabric. *American Journal of Science*, *263*(4), 289–301. https://doi.org/10.2475/ajs.263.4.289
Zamani, B. G., Angelier, J., & Zamani, A. (2008). State of stress induced by plate convergence and stress partitioning in northeastern Iran, as indicated by focal mechanisms of earthquakes. *Journal of Geodynamics*, *45*(2-3), 120–132. https://doi.org/10.1016/j.jog.2007.07.003
Zanchi, A., Berra, F., Mattei, M., Ghassemi, M. R., & Sabouri, J. (2006). Inversion tectonics in central Alborz, Iran. *Journal of Structural Geology*, *28*(11), 2023–2037. https://doi.org/10.1016/j.jsg.2006.06.020
Zanchi, A., Malaspina, N., Zanchetta, S., Berra, F., Benciolini, L., Bergomi, M., … Kouhpeyma, M. (2015). The Cimmerian accretionary wedge of Anarak, Central Iran. *Journal of Asian Earth Sciences*, *102*, 45–72. https://doi.org/10.1016/j.jseaes.2014.08.030
Zanchi, A., Zanchetta, S., Garzanti, E., Balini, M., Berra, F., Mattei, M., & Muttoni, G. (2009). The Cimmerian evolution of the Nakhlak–Anarak area, Central Iran, and its bearing for the reconstruction of the history of the Eurasian margin. *Geological Society, London, Special Publications*, *312*(1), 261–286. https://doi.org/10.1144/SP312.13
Zarifi, Z., Nilfouroushan, F., & Raeesi, M. (2013). Crustal stress map of Iran: Insight from seismic and geodetic computations. *Pure and Applied Geophysics*, *171*(7), 1219–1236. https://doi.org/10.1007/s00024-013-0711-9
Ziegler, P. A., van Wees, J. D., & Cloetingh, S. (1998). Mechanical controls on collision-related compressional intraplate deformation. *Tectonophysics*, *300*(1-4), 103–129. https://doi.org/10.1016/S0040-1951(98)00236-4

Erratum

In the originally published version of this article, Figure 9 contained an incorrect picture in 9c. The figure has since been corrected, and this version may be considered the authoritative version of record.